SCIEPublish

Review

A Comprehensive Review towards Oxidation Resistant Press-Hardened Steels

Zhao Li [1], Lingyu Wang [1,*], Zhou Wang [2], Jianfeng Wang [2] and Wei Xu [1]

[1] State Key Laboratory of Rolling and Automation, Northeastern University, Shenyang 110819, China; lizhlut@126.com (Z.L.); xuwei@mail.neu.edu.cn (W.X.)

[2] China Science Laboratory, General Motors Global Research & Development, Shanghai 201206, China; zhou.wang@gm.com (Z.W.); jeff.wang@gm.com (J.W.)

* Corresponding author. E-mail: wanglingyu@ral.neu.edu.cn (L.W.)

Received: 25 January 2025; Accepted: 26 February 2025; Available online: 6 March 2025

ABSTRACT: As an important lightweight material, press-hardened steels (PHS) are now widely used in the car body-in-white. However, severe oxidation of conventional Mn–B bare sheets not only damages production molds, but also prevents subsequent welding and painting, leading to a significant increase in production costs. The aim of this review is to systematically summarize the current solutions to overcome the problem of high-temperature oxidation of conventional Mn–B PHS and to highlight future directions for improvement. The review begins with a brief background on PHS, followed by a detailed description of measures to improve the oxidation resistance of conventional Mn–B PHS and the development of novel PHS with superior oxidation resistance. The oxidation resistance solutions for conventional Mn–B PHS mainly include the use of coatings and pre-deposited films. In contrast, the oxidation resistant PHS mainly includes the use of the oxidation resistant elements Cr, Si, Al or rare earth elements to improve the steel's own high-temperature oxidation resistance.

Keywords: Press-hardened steel; High-temperature oxidation; Coating; Oxidation resistance; Hot stamping

1. Introduction

With the significant growth in commercial vehicles, CO_2 from transportation is the second largest source of emissions after electricity generation, and approximately 90% of these transportation emissions come from automobiles [1]. This has made energy conservation and emission reduction a key goal for the automotive industry. Lightweighting is currently one of the most direct and effective ways to save energy and reduce emissions. Some researchers have shown that there is a linear relationship between vehicle weight and fuel consumption [2]. Taking passenger cars as an example, if the weight of a vehicle is reduced by 10%, the fuel consumption and emissions of the car will be reduced by 6% [3,4]. To comply with increasingly stringent carbon emission regulations and crashworthiness standards [5,6], efforts are being made to reduce vehicle weight without compromising passenger safety. Therefore, the pursuit of strong yet lightweight materials remains a pivotal research focus within the automotive industry. The low density and resultant lightweighting of magnesium and aluminum alloys, when compared to steel, render them highly attractive for weight reduction purposes. Specifically, materials such as AZ31 magnesium alloy and the 6xxxx series have been partially incorporated into the car body-in-white (BIW) [7,8]. Nevertheless, their widespread adoption has been hindered by factors such as poor formability, manufacturing challenges, elevated costs, and reduced strength. Consequently, the current automotive lightweighting strategy primarily relies on the development and deployment of advanced high-strength steels (AHSS). The proportion of AHSS utilized in the BIW serves as a key metric for evaluating automotive lightweighting efforts [1]. The advancement and deployment of high-performance AHSS are crucial for the sustainable growth of the automotive industry.

Press-hardened steels (PHS) have received widespread attention as an important category of AHSS. As shown in Figure 1a, PHS is widely used in critical components such as A–pillars, -pillars, bumper beams, door beams, front rails,

https://doi.org/10.70322/htm.2025.10004

side-cross members and tunnels to achieve lightweighting while improving the overall crashworthiness of vehicles. Studies have shown that PHS exhibits superior anti-intrusive crash performance compared to other automotive steels, both at low and high strain rates [9]. Over the past two decades, hot-stamped parts have undergone rapid development, although they were first used in mass-produced passenger cars as early as mid-1980s [10]. The global demand for hot-stamped parts increased from 27.6 million in 2000 to 127.3 million in 2010 and continues to grow to a forecast value of 586.2 million in 2018 (Figure 1b) [10]. According to related reports, global demand for PHS will reach around 6 million tons in 2023, up from 3 million tons in 2018 [11]. At the same time, the mass proportion of PHS in BIW has increased significantly from 19% in 2005 to 38% in 2016 [10,12], as shown in Figure 1c. Furthermore, PHS is currently "the leader in automotive lightweighting" due to their impressive strength in the classical strength and total elongation diagram (Figure 1d) [13]. In terms of tensile strength, the grades of first-generation AHSS are ranked by tensile strength and, in rough order from low to high, are interstitial-free (IF) steels, mild steels, bake-hardening (BH) steels, carbon-manganese (C–Mn) steels, high-strength low-alloy (HSLA) steels, transformation-induced plasticity (TRIP) steels, dual-phase (DP) and complex-phase (CP) steels, martensitic (MART) steels, and PHS. Notably, PHS also exceeds the strength of second- and third-generation AHSS, including twinning-induced plasticity (TWIP) steels and quench-and-partition (Q&P) steels, respectively [14]. In addition, PHS can reach strengths ranging from 1500 MPa to more than 2000 MPa, which has a wider application in BIW components in the automotive industry.

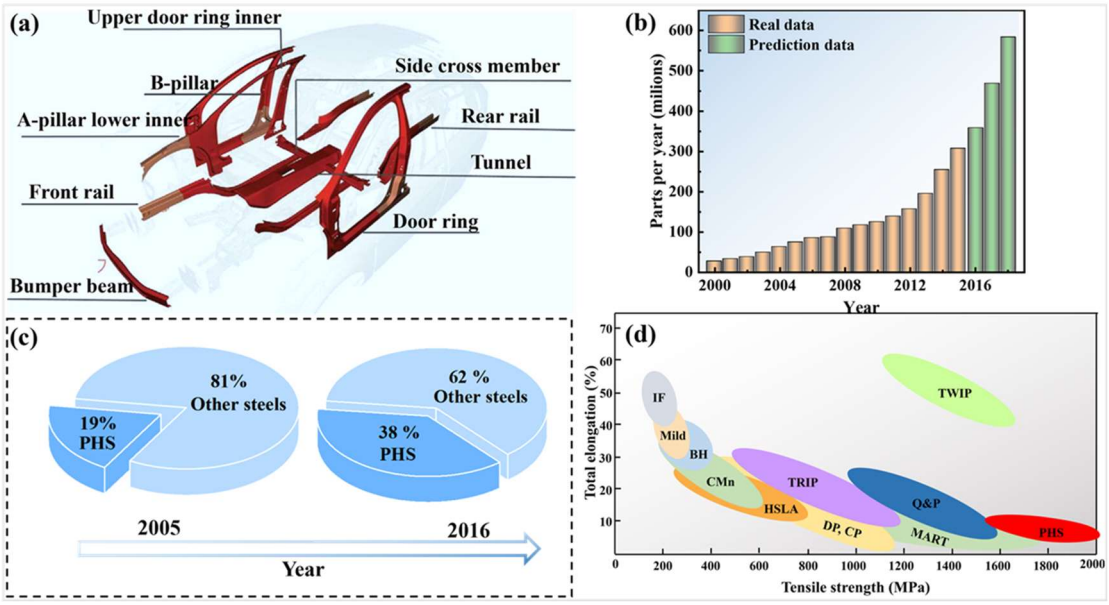

Figure 1. Status of PHSs for industrial applications: (**a**) Application of hot-stamped parts on a BIW 10, (**b**) Demand for hot-stamped parts in the global automotive industry (adapted from [13]), (**c**) the mass proportion of PHS for the automotive industry (re-created after [10,12]), and (**d**) A comparison of the strength and elongation properties of various advanced high strength steels (adapted from [13]).

Thin, high-strength steels pose a considerable challenge for conventional cold-forming processes, owing to the increased susceptibility of body parts to cracking and excessive spring-back during the forming stage. This, in turn, has an adverse impact on body assembly. Specifically, when the tensile strength surpasses 1.2 GPa, it becomes increasingly difficult to produce body parts with intricate structures and shapes via cold forming, thereby limiting the application of higher strength steels [15]. However, hot stamping, alternatively termed press-hardening, offers a viable solution to these challenges. This advanced forming technique is an integrated process that combines thermomechanical forming and heat treatment, ensuring high dimensional accuracy of the components while imparting ultrahigh strength. Additionally, it boasts numerous advantages, such as high forming rates and extended die life [16]. Prior to the hot stamping process, the sheets are heated to 900–950 °C and held for a duration of 3–10 min to achieve complete austenitization. Subsequently, the steel sheets are swiftly transferred by a robotic arm to a die equipped with a cooling system, where they undergo hot deformation and quenching to complete the austenite-to-martensite transformation [17,18]. Due to the practical difficulties associated with conducting real hot stamping experiments under laboratory settings, laboratory investigations of most PHS typically simulate the hot stamping process through direct austenitization and flat die quenching, as depicted in Figure 2a [19]. As a consequence of the hot forming procedures, high-temperature oxidation of the steel plate is inevitable. Despite the utilization of inert gases (Ar/N_2 and sometimes

NH_3) to safeguard the steel plate during the austenitizing stage, oxygen infiltration from the external atmosphere remains unavoidable. From Figure 2b, it can be seen that a thick and easily peelable oxide layer formed on the surface of the Mn-B bare sheet (e.g., 22MnB5) after hot stamping, indicating that severe high-temperature oxidation inevitably occurred during hot stamping [20–23]. As a result, the oxide scale detaches during the stamping process, damaging the die and reducing its service life. This not only increases production costs but also reduces shape accuracy and may even cause part deformation [24–28]. In addition, due to the highly oxidized nature of the 22MnB5 sheet, its hot stamped parts must be shot peened before entering the automotive assembly plant for subsequent welding and painting processes, which further elevates production costs. Initially, 22MnB5 PHS are carbon (C–) and manganese (Mn–) alloyed steels with small amounts of boron (B–) added for hardenability [10,29,30]. For example, a typical commercial 22MnB5 grade has a basic chemical composition of 0.19~0.25 wt.% C, 1.1~1.4 wt.% Mn, 0.001~0.005 wt.% B, and contents of chromium (Cr) and silicon (Si) are usually less than 0.5 wt.% [10,31]. It is evident that the 22MnB5 steel was not developed with the specific intention of resisting high-temperature oxidation. Consequently, the formation of an oxide scale and surface decarburization during the hot stamping process is an unavoidable consequence. The heat treatment temperature of DP is below the austenitizing temperature (Ac_3), whereas the austenitizing temperature of PHS is above Ac_3, so the degree of oxidation of DP steels is relatively low compared to that of PHS. The heat treatment temperature of transformation-induced plasticity (TRIP) is also higher than the austenitizing temperature and the oxidation resistance challenge is similar to that of PHS. However, the continuous annealing time is much shorter than the one for press hardening. The many challenges posed by the severe oxidation of PHS during hot stamping make it particularly important that they have some oxidation resistance.

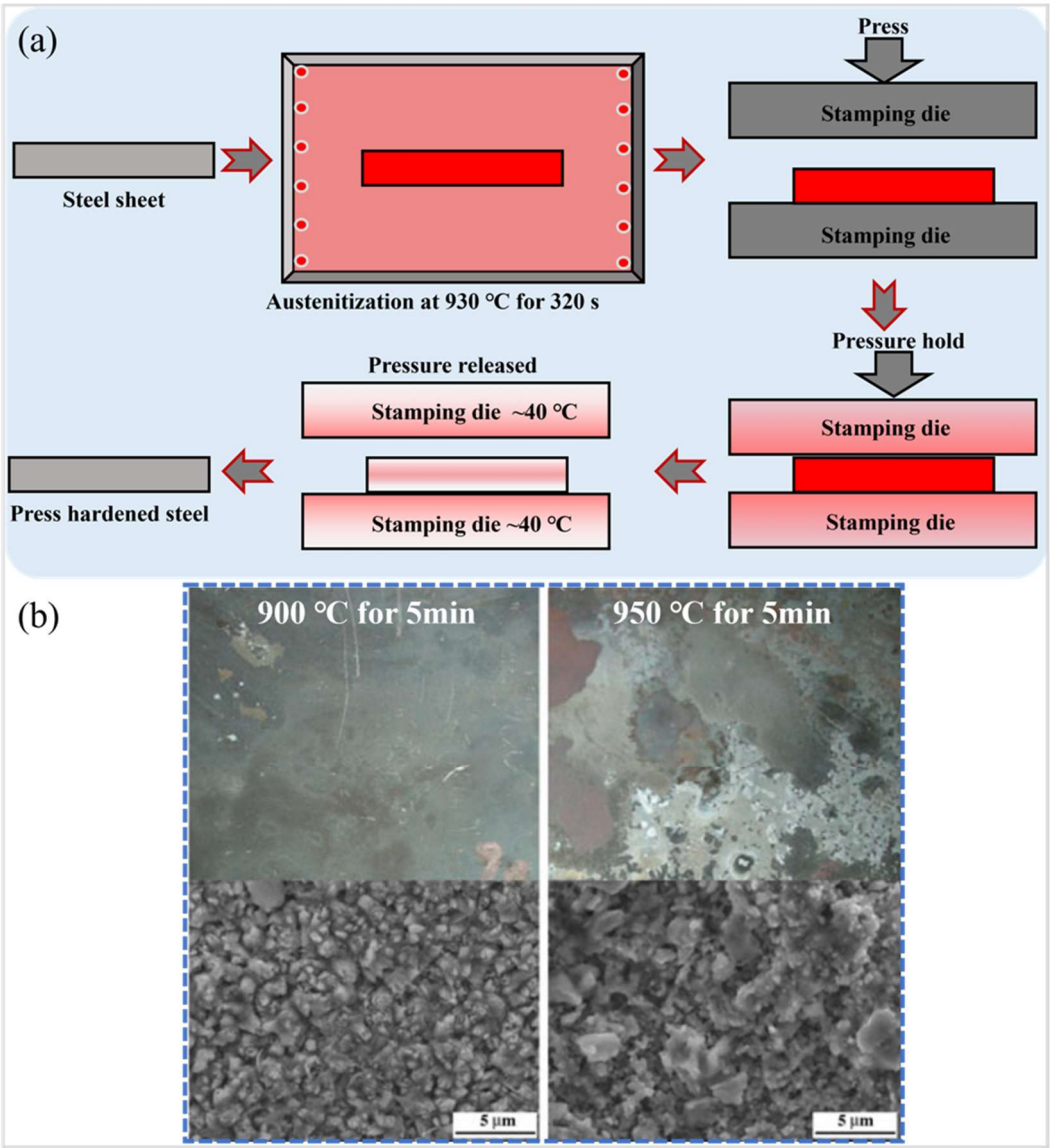

Figure 2. (**a**) Schematic diagram of the hot stamping under laboratory conditions (re-created after [18]), and (**b**) Surface morphology of 22MnB5 bare plate after heat treatment at different temperatures [23].

Currently, high-performance PHS can be broadly categorized into conventional Mn–B steels (both with and without coatings) and newly developed oxidation-resistant PHS. A comprehensive review of their microstructure, mechanical properties, bending characteristics, and impact resistance has been conducted in the existing literature [13]. Consequently, this review primarily focuses on the efficacy of coatings and pre-deposited films for conventional Mn–B steels in enhancing their high-temperature oxidation resistance. In contrast, for oxidation-resistant PHS, this review examines the influence of composition and pretreatment on their oxidation resistance. The objective of this review is to provide a reference and foundation for related research endeavors and applications, ultimately contributing to the sustainable development of high-performance oxidation-resistant PHS.

2. Conventional Mn–B Steels

2.1. Coating Sheets

The principal coatings developed for application to PHS with the objective of preventing high-temperature oxidation are Al–Si coatings, Zn-based coatings, and other coatings [32]. A comprehensive examination of this topic will be presented in the following sections.

2.1.1. Al–Si Coatings

After an extended development period, the Al–Si coating has become the most prevalent protective coating for PHS, with a typical composition of 87 wt.% Al, 10 wt.% Si, and 3 wt.% Fe [33–35]. Presently, the fabrication of automotive components, such as A-pillar reinforcement plates, B-pillar reinforcement plates, and door impact beams, involves the utilization of Al–Si coated PHS [36]. The coating is applied via the hot-dip plating process at 670 °C, resulting in a pre-coated layer with a thickness of 20 to 33 μm [37–39]. Figure 3a depicts the scanning electron microscope (SEM) image of the cross-section microstructure of the hot-dip Al–Si coating layer prior to austenitization. The cross-sectional microstructure of hot-dip Al–Si coating is primarily comprised of three distinct layers, as shown in Figure 3b. The outermost layer is a pure Al layer. The middle layer is constituted by an Fe-Al-Si ternary alloy phase. The innermost layer is an Fe–Al alloy layer, which is predominantly composed of $FeAl_3$ and Fe_2Al_5. Additionally, a layer of Fe_2SiAl_7 (τ_5 phase), with a thickness of approximately 5 μm, is present between the matrix and the Al–Si coating layer [40]. Figure 3c,d demonstrate the coating microstructure of the Al–Si coated sheet following austenitization (heat treatment at 930 °C for 6 min) and hot stamping. The final microstructure of the coating layer is primarily divided into five layers (with the outermost layer being the first): The initial and third layers are composed of $FeAl_2$, the second and fourth layers are the Fe_2SiAl phase, and the fifth layer is constituted by an Al and Si-rich α-Fe phase, as reported in relevant studies [41,42]. The oxidized weight gain of 22MnB5 steel with Al-Si coating exhibited minimal variation at 900 °C after a short period (≤8 min) of austenitization. Furthermore, the oxygen diffusion depth in the coating is less than 4 μm, which is significantly smaller than the actual thickness of the coating, indicating that the Al-Si coating can effectively protect the steel matrix during austenitization [41]. The diffusion rate of Al atoms in the Fe_2SiAl_2 and coating/steel substrate interface diffusion layers during austenitization is much higher than that for Fe atoms, so that Al atoms diffuse inward to form the Fe–Al alloy phase and outward to form the Al_2O_3 layer [43–45]. The formed Al_2O_3 can effectively inhibit the mutual diffusion of oxygen and iron, thus effectively protecting the steel matrix.

Al–Si coated sheets do not require protective gases during heating, nor do they require subsequent shot peening. Additionally, no oxide scale remains on either the product surface or the mold surface, thereby addressing the issues of oxidation and decarburization that arise on the surface of uncoated PHS. However, the diffusion of the Al–Si coating is a process that is dependent on time. If the diffusion is incomplete due to shorter heating times of the blank, or if it is overly sufficient, resulting from prolonged heating, the weldability of the component and the surface properties of the coated part will be compromised [46,47]. Consequently, there exists a direct correlation between the thickness of the coating and the duration required for the Al–Si blank to undergo austenitization, which subsequently influences productivity. Furthermore, an augmentation in coating thickness leads to a decrement in the efficiency of the hot-dip plating process and an increment in the cost of the alloy. The increased thickness of Al–Si coatings may also be susceptible to coating droplets sticking to ceramic rollers in the furnace, resulting in a deterioration of product quality and further elevated production expenditures [48]. Last but not least, flexural toughness is one of the most important indicators of the safety of automotive components, but thicker Al–Si coatings are detrimental to this property [49]. In recognition of the disadvantages associated with thicker Al–Si coatings, recent years have witnessed the development of a relatively thin Al–Si coating, with a thickness ranging from 13~19 μm [50–52]. Structural analysis of this thin Al–Si pre-coating revealed that the thickness of the intermetallic compounds was roughly comparable to that of the thicker

Al–Si coating, with the primary difference being a notable thinning of the Al coating. In addition, the thin Al–Si pre-coatings were found to significantly mitigate the degree of carbon enrichment in the vicinity of the coating-substrate interface (i.e., the side close to the substrate), thereby effectively enhancing the crash toughness of the hot-formed parts. Undoubtedly, a thinner Al–Si coating thickness will result in a reduction in coating costs, as well as facilitate rapid heating of realistic steel sheets.

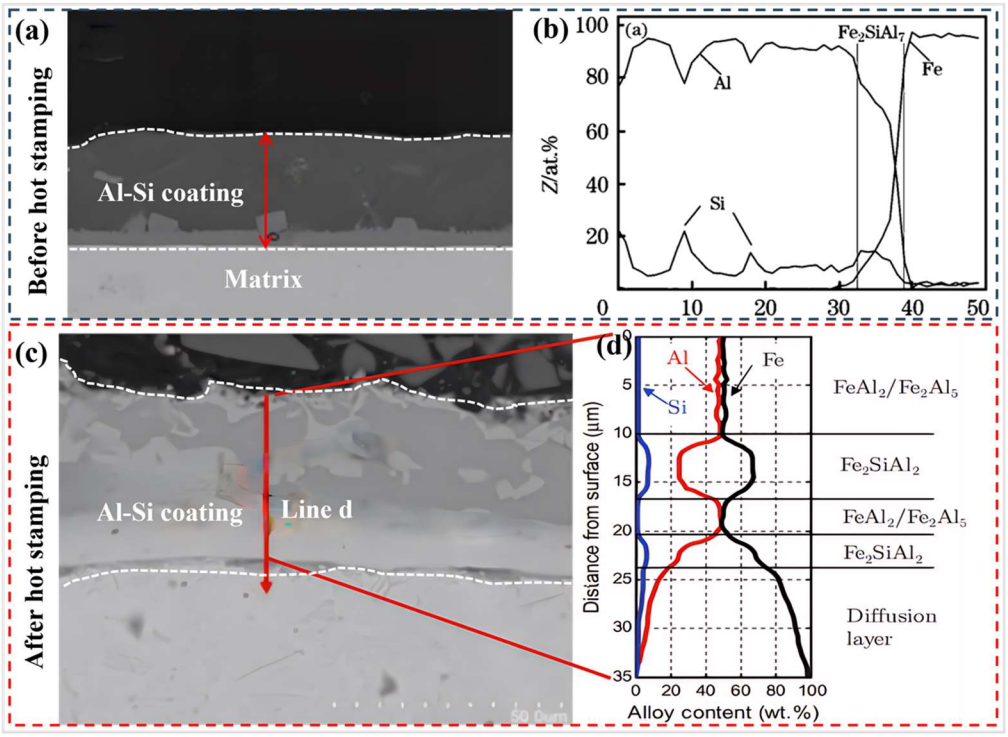

Figure 3. (**a**) SEM image of the cross-section microstructure of hot-dip Al–Si coating before hot stamping, (**b**) Analytical results of energy-dispersive spectroscopy (EDS) of hot-dip Al–10%Si coatings before austenitization [40], (**c**) SEM cross-section of Al–Si coated sheets after austenitizing and hot stamping of the coating microstructure, (**d**) EDS line scan analysis corresponding to (**c**) [41].

However, both thick and thin Al–Si coatings are unable to provide cathodic protection due to their very close electrochemical potential to the substrate. Consequently, Al–Si coated sheets offer only limited corrosion protection after hot stamping, and are primarily utilized in the dry area of the BIW [53]. However, in view of the extensive use of PHS in BIW, there has been a gradual shift toward using PHS in wet zones, particularly in the chassis and suspension. This development underscores the urgent need for effective cathodic corrosion protection measures.

2.1.2. Zn-Base Coatings

Zn-based coatings not only protect the substrate from oxidation during the hot stamping process but also impart superior corrosion resistance to the components after hot stamping. Therefore, galvanized PHS is also a popular alternative to Al–Si coatings. Presently, Zn-based coatings employed as protective layers for PHS primarily consist of hot-dip galvanized Zn (GI) coatings and alloyed Zn–Fe (Galvannealed coating, GA) coatings. The GI coatings are basically pure Zn containing 0.2–2.5 wt.% Al, while GA coating contains Fe with a mass fraction of approximately 10–15% [54–56]. GI-coated sheet comprises two layers prior to hot stamping: an external Zn coating and a thin Al-rich layer at the substrate interface (Figure 4a) [41]. Iron diffusion occurs during heating, so a three-layer structure is formed after hot stamping [56,57]. The outermost layer is an oxide layer consisting of Zn and Al oxides, which prevents Zn evaporation. The middle layer is the Zn-rich Γ phase, which plays a pivotal role in corrosion resistance (contains a minimum of 70 wt.% Zn). At the interface of the matrix is the α-Fe phase, which contains at least 10 wt.% Zn.

However, the application of Zn-based coatings is often accompanied by a significant challenge: the occurrence of liquid metal embrittlement (LME) [58–60]. Given that the melting point of Zn is approximately 420 °C, which is considerably lower than the forming temperature employed in hot stamping, this phenomenon occurs when the matrix is subjected to stress (Figure 4b). As illustrated in Figure 4c, the ingress of liquid Zn into the matrix through the compromised coating leads to the formation of cracks in the substrate's surface layer. These surface cracks, known as

microcracks, propagate along the austenite grain boundaries, eventually leading to premature cracking of the matrix [54,61]. Furthermore, it has been established that when microcracks exceed 10 μm, a substantial decrement in fatigue stress occurs [22]. Bhattacharya et al. used intercritical annealing (partial austenitization) to form a dual-phase microstructural variant in the same steel, thereby suppressing LME [62]. This is due to the fact that the dual-phase microstructure consists of ultrafine ferrite grains and discrete martensitic islands, as well as smaller area fractions of prior austenite grain (PAG) boundaries, which reduces the susceptibility of DP steels to LME. Cho et al. found that intergranular cracking is due to the penetration of the liquid zinc alloy phase along the grain boundaries at the crack tip, propagating over the prior austenite grain boundaries, which is weakened by the zinc diffusion mitigating the phase transition to ferrite [63]. As demonstrated in Figure 4d, Zn–based coatings exhibit a distinct disadvantage in that they possess a narrower hot-forming process window compared to bare sheets and those coated with Al–Si. This is attributed to the boiling point of pure Zn (907 °C) being very close to the temperature of the austenitizing stage (880 °C for 22MnB5) in the hot stamping process. However, the duration of the low-temperature austenitization is insufficient for the completion of coating diffusion. Conversely, an excessively long duration leads to the formation of deeper microcracks within the base metal [10,64,65]. Consequently, the utilization of Zn-based coatings in PHS is constrained. Recently, Zn–Mg coatings have been widely used for their superior corrosion resistance over Zn coatings [66]. Since Mg atoms are preferentially ionized to provide electrons to the steel substrate, which can enhance the effectiveness of the sacrificial anode. Mg-containing corrosion products such as $MgCO_3$ and $Mg(OH)_2$ are formed on the surface during the corrosion process, thereby delaying corrosion and improving the protective ability of the coating. intermetallic phases of Mg and Zn, such as Mg_2Zn_{11} and $MgZn_2$, have higher corrosion resistance.

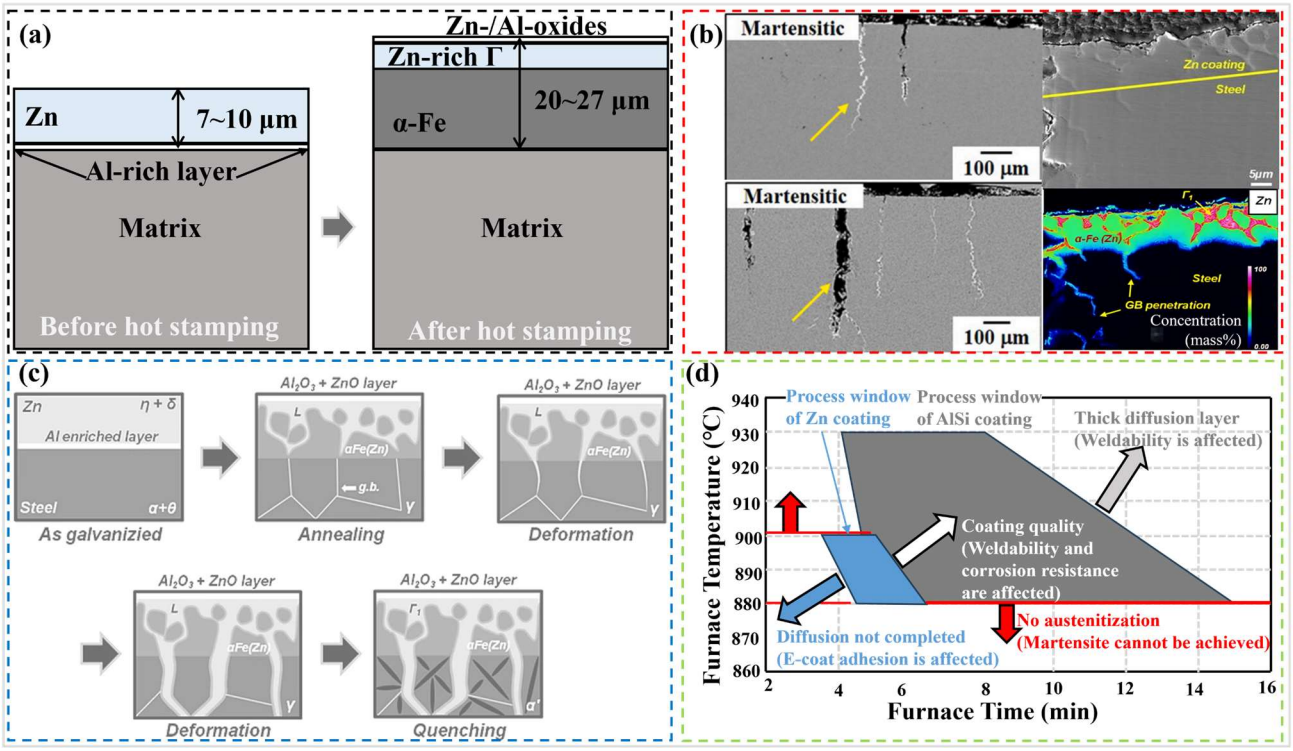

Figure 4. (**a**) Schematic of Zn (GI) coating before and after hot stamping (adapted from [41]), (**b**) Cross-sectional morphology of LME cracks [54,62], (**c**) The process of LME occurrence during hot stamping of Zn-coated steels [53], and (**d**) Processing window of the hot stamping process for Zn and Al–Si coatings (adapted from [41]).

2.1.3. Other Coatings

Varnish coatings have been demonstrated to alleviate oxidation and decarburization of bare sheets during the hot stamping process. The varnish coating, which was developed and implemented by Nano–X in 2005, is a paint-like coating that can be directly applied to the bare sheet surface using a spray gun or paint roller, as illustrated in Figure 5 [41,67]. Compared to bare sheets, the side with a varnish coating on the surface has better oxidation resistance, and there is no significant peeling of the oxide layer. To date, Nano–X has developed two generations of varnish coatings. The first-generation x-tec varnish coating is a composite of organic and inorganic materials, aluminum powder, graphite, and wax. This coating, which is 6–7 μm thick, is applied to bare sheets but must be removed by sandblasting prior to

soldering. The subsequent generation of x-tec varnish coatings has undergone enhancements that permit welding without the necessity of sandblasting for coating removal. X-tec coatings exhibit better lubrication conditions and lower friction compared to Al–Si coatings. At the same time, x-tec coatings possess high heat-absorbing capabilities and do not necessitate additional diffusion time, thereby reducing the holding time of the slab in the furnace. Furthermore, they can be accommodated for inductive, conductive, and near-infrared heating methods [22]. However, this coating cannot be deformed during the heating process and has poor corrosion resistance. In 2015, Henkel also introduced a varnish coating for hot stamping, termed Bonderite S–FN 7500 PH. This coating can be adapted to rapid heating and provides corrosion and oxidation protection. Although the coefficient of friction for this coating has not been publicly disclosed, it aids in lubricating the blank, and the coating does not require sandblasting for removal prior to spot welding [68].

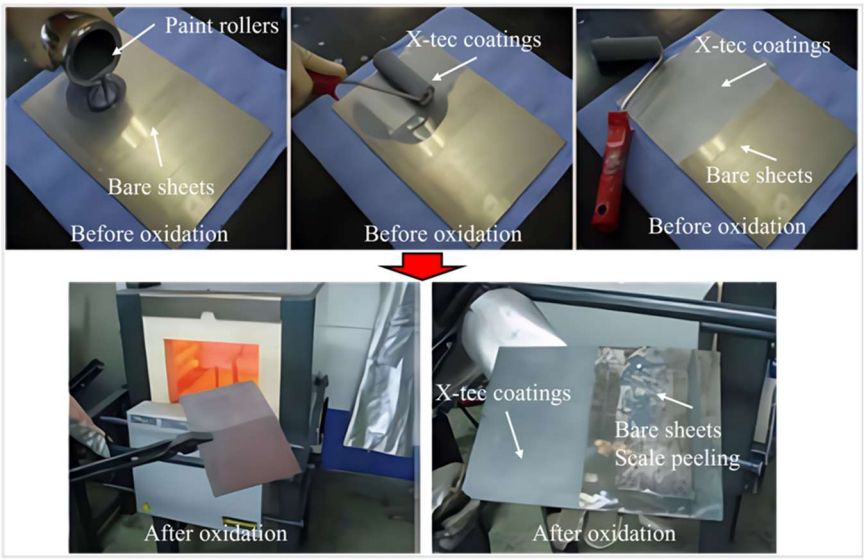

Figure 5. The x-tec coatings can be applied using a spray gun or paint roller to cover the surface of bare sheets as well as the macroscopic morphology after hot stamping (adapted from [41]).

An anti-oxidizing oil coating has been developed specifically for application on bare PHS. This coating can be categorized into two primary types: one comprises fatty acids for the formulation of soaps, carbonate-based solid lubricants, and chelating agents; the other consists of boric acid, phosphate-based solid lubricants, fatty acids utilized in oil-based soaps, metal soaps, and chelating agents. While this coating provides effective oxidation protection and facilitates easy removal after heating, it exhibits suboptimal corrosion resistance [69].

To meet the requirements of hot stamping steels for oxidation resistance and a wide heating window, Thyssen has developed the Gamma Protect plating technology [70]. The coating constitutes an electroplated Zn–10Ni layer, characterized by a single-phase γ–Ni5Zn21 metal compound within the layers microstructure proximal to the substrate. This phase makes the melting point of the coating reach 880 °C, which effectively avoids the LME phenomenon of Zn–based coatings. In addition, the incorporation of the Ni element serves to stabilize the Zn–rich phase, enabling the coating to possess a relatively extensive thermal processing window (880~920 °C). The oxide layer formed on the Zn–Ni surface exhibits greater stability compared to galvanized layers, effectively inhibiting the volatilization of Zn from the surface. At the same time, the combination of the surface oxide layer and the stable γ-phase makes the coating possess good friction properties. Although the comprehensive performance of this coating is excellent, its high cost and low productivity make it not widely used.

Based on the above discussions, a concise summation of the utilization of coatings to address the oxidation issue in PHS can be derived. Firstly, while all coatings offer protection against oxidation, they inherently possess certain limitations. Secondly, Al–Si coatings are currently the most prevalent, albeit at a significant cost. Lastly, a coating sheet that balances excellent overall performance with cost-effectiveness remains elusive.

2.2. Pre-Deposited Films

Apart from surface coatings, the preparation of pre-deposited or passivated films on the steel surfaces can also protect the metal substrate during the high-temperature oxidation phase. Notably, surface pre-deposited films are more cost-effective than surface coatings. Du et al. investigated the effect of molybdate passivation films on the high-temperature oxidation properties of PHS1500 hot-formed steel (Table 1) [70]. The pre-passivation films, with

thicknesses of 2.87 and 3.03 nm, were fabricated by immersing the experimental steel in a 1 g/L Na_2MoO_4 solution for durations of 15 (sample 2) and 30 min (sample 3) at room temperature, as illustrated in Figure 6a. The oxidation rate constants for sample 1 (un-passivated sample), sample 2, and sample 3 were 22.8, 16.03, and 14.74 $mg^2cm^{-4}min^{-1}$, respectively (Figure 6b). The excellent high-temperature oxidation resistance exhibited by the passivated samples can be attributed to the fact that the pre-passivation film hinders the oxidation of the metal substrate at the early stage of oxidation, resulting in a large amount of Si enriched on the surface of the metal substrate [71,72]. As the oxidation proceeds, the pre-passivation film is damaged, resulting in the oxidation of Si to form a large amount of SiO_2, which further reacts with FeO to form Fe_2SiO_4. As shown in Figures 6c,d, the passivated sample formed a dense Fe_2SiO_4 layer during the oxidation process, while the un-passivated sample formed a defective Fe_2SiO_4 layer. Therefore, the passivated samples have higher antioxidant performance.

Table 1. Chemical compositions (wt.%) of the PHS1500 steels.

Steel	C	Mn	Si	Al	Cr	Ti	B	S	Ref.
1500PHS	0.215	1.46	0.238	0.037	0.057	0.029	<0.01	0.0035	65
1500PHS	0.24	1.40	0.20	-	-	-	0.02–0.05	-	68

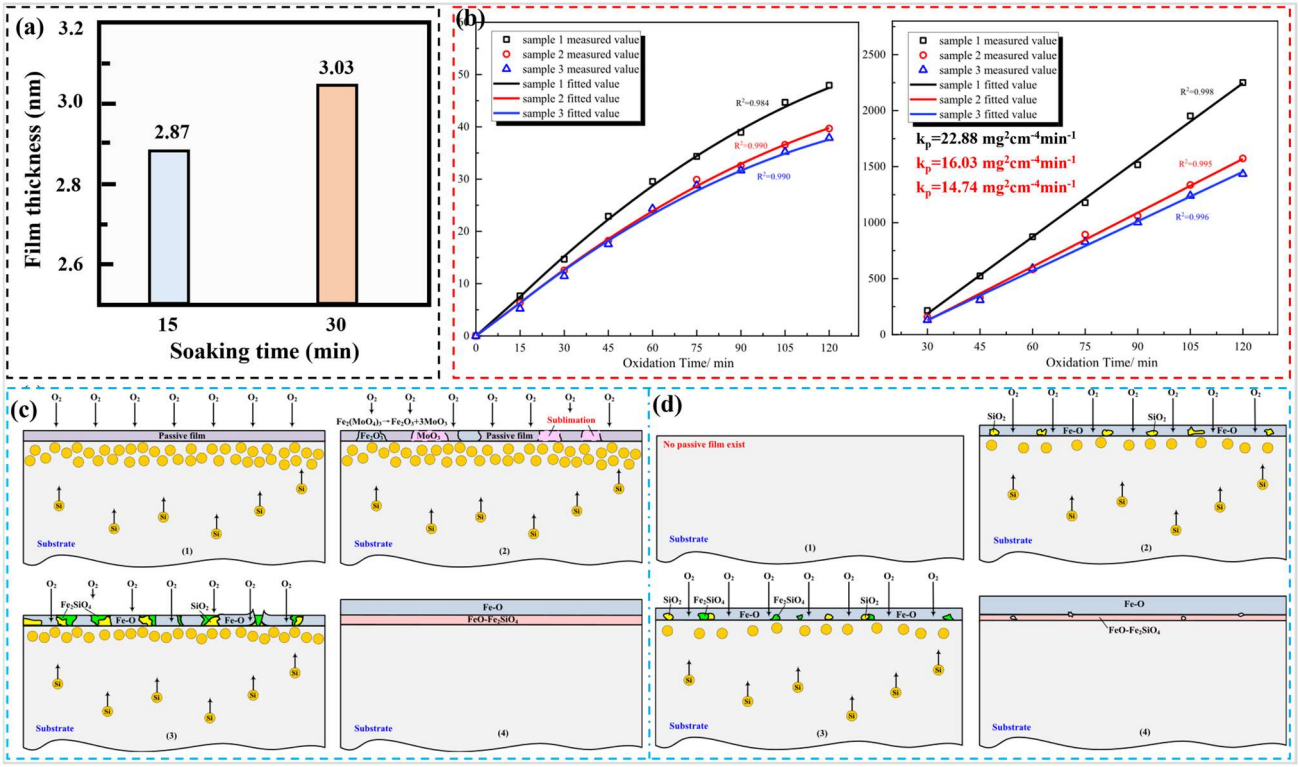

Figure 6. (**a**) Thickness of pre-passivated film (adapted from [70]), (**b**) Oxidation kinetic curves for un-passivated and passivated samples at 930 °C, (**c**) Schematic representation of the oxidation process of the passivated sample, and (**d**) Schematic representation of the oxidation process of the un-passivated sample ((1)–(4) in the figure represent the order of oxidative evolution) [70].

Nie et al. enhanced the high-temperature oxidation resistance and oxide adhesion of the PHS1500 steel (Table 1) in an Ar + 0.1 vol% O_2 gas mixture at 930 °C for a duration of 20 min, by preparing a pre-deposited film through the addition of silicate-molybdate to the rinse solution after pickling (Figure 7a) [73]. The concentrations of silicates and molybdates in the pretreatment solution are detailed in Table 2. As demonstrated in Figure 7b, the antioxidant properties of the pretreated samples were all superior to those of the untreated sample (S0), with sample S3 exhibiting the most notable antioxidant properties. The silicate in the pre-deposited film effectively impeded the mutual diffusion of Fe^{2+} and O^{2-}, owing to its low ionic conductivity [74,75]. Consequently, the growth of the FeO layer on the surface of the pretreated sample was significantly hindered and the antioxidant performance was enhanced, as demonstrated in Figure 7c. Furthermore, molybdate has been shown to be capable of filling the space between silicate precipitate, thereby increasing the compactness of the pre-precipitated film.

While the pre-deposited film on the surface of PHS has been demonstrated to enhance its antioxidant performance at elevated temperatures, it remains at the laboratory research stage. The applicability and compatibility of this film in actual industrial production are yet to be determined. Pre-deposited films can be prepared industrially by adding silicates

or molybdates to the rinse solution of the pickling line. Therefore, it is hypothesized that the preparation of the pre-deposited films can have good compatibility with the pickling lines of existing industries. In addition, silicates and molybdates are relatively low-cost and therefore having better economics for industrial production.

Table 2. Concentrations of silicate and molybdate in the rinse solution [73].

Solution No.	S1	S2	S3	S4
Na_2SiO_3 (mg/L)	500	1000	500	1000
Na_2MoO_4 (mg/L)	0	0	200	200

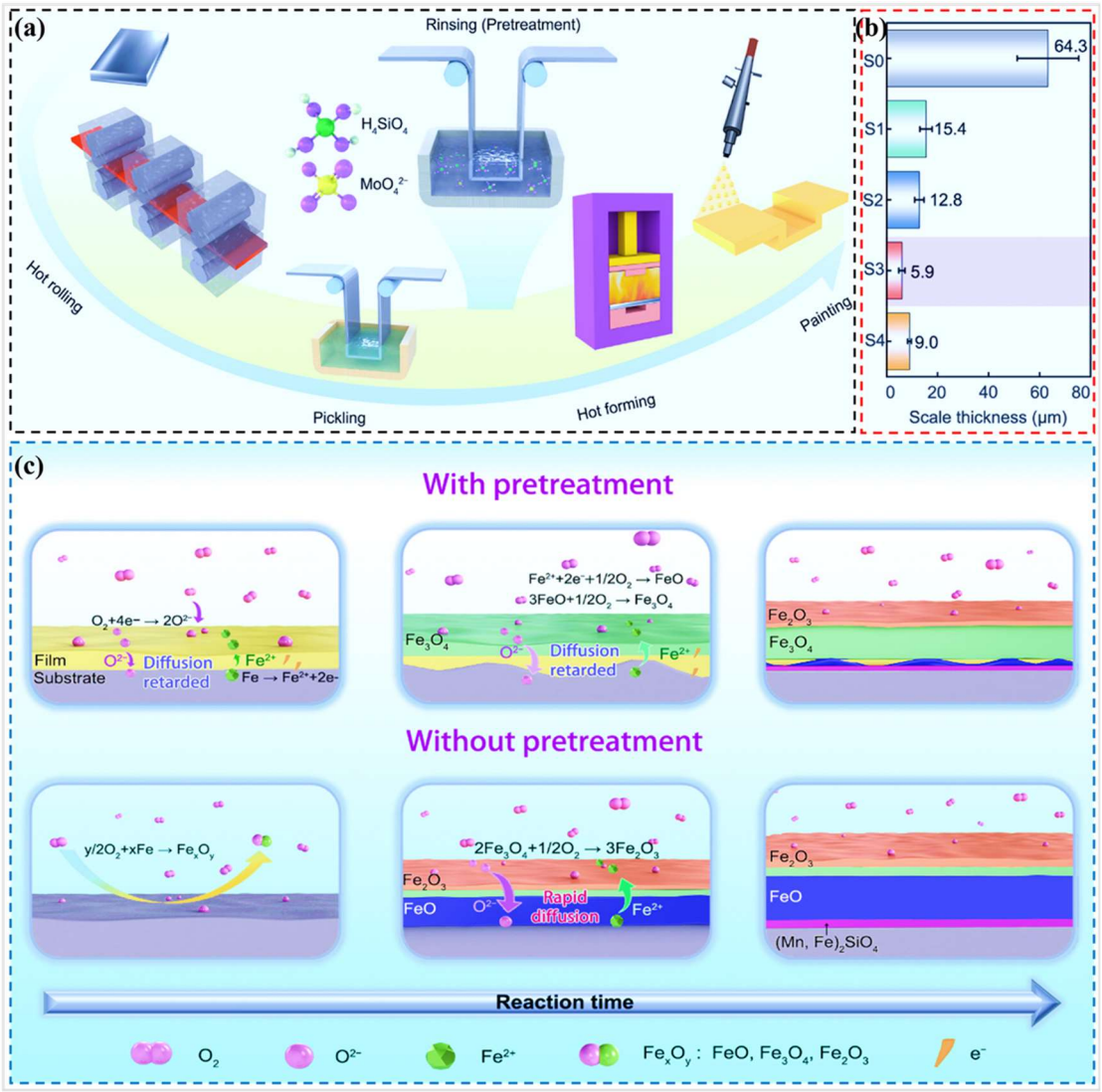

Figure 7. (**a**) Schematic diagram of the process of PHS (Since the pretreatment solution is an aqueous solution, the silicates are mainly H_2SiO_4), (**b**) Oxidation thickness of without pretreated and pretreatment samples at 930 °C for 20 min, and (**c**) Schematic representation of the oxidation process of pretreated and unpretreated samples during the holding phase of austenitizing [73].

3. Oxidation-Resistant PHS

The accelerated evolution of PHS has concurrently led to a diversification in material design, with novel PHS designs incorporating moderate quantities of single or multiple antioxidants alloying elements, such as Cr, Si and Al, in contrast to conventional 22MnB5 steels. These antioxidant alloying elements possess the ability to form a dense oxide film on the steel surface at elevated temperatures, thereby shielding the base metal from environmental exposure and providing a protective effect. It is acknowledged that the addition of these alloying elements can also lead to enhancements in other properties, such as mechanical properties [13]. However, the focus of this review is solely on their role in enhancing the antioxidant properties of PHS. Consequently, a comprehensive understanding of the role of antioxidant alloying elements in the high-temperature antioxidant resistance of novel PHS is imperative for the advancement of this field. The following sections are discussed in terms of the amount of alloying elements added to

antioxidant hot-forming steels from high to low.

3.1. Hot-Formed Stainless Steels

It is well known that the higher the Cr content, the better the high-temperature oxidation resistance of stainless steels, such as 310S, 304L and 317L stainless steels (Cr ≥ 18 wt.%). For this reason, Santacreu et al. first applied this concept in the high-temperature oxidation of conventional PHS. Presently, hot-formed stainless steels suitable for use in hot stamping lines exhibit Cr contents ranging from approximately 11–13 wt.%, with their chemical compositions shown in Table 3. Notably, the Max1.2 hot-formed stainless steel, developed by Aperam, demonstrated an absence of black oxide scale on its surface. Instead, it formed a golden-yellow appearance following industrial trial production for B-pillars (Figure 8a). This observation underscores its exceptional oxidation resistance [76,77]. Max1.2 does not necessitate the application of coatings or the use of inert atmosphere protection during hot stamping [77,78]. Furthermore, the martensitic phase transition temperature of Max1.2 is much lower than that of 22MnB5 steel (Figure 8b) due to the ability of Cr to increase the hardenability of the steel, allowing more manipulation of the time of transfer from austenitizing to the mold, thus ensuring product stability [78].

Although hot-formed stainless steels have excellent oxidation resistance, their high Cr content undoubtedly leads to deterioration in production costs and welding performance. Therefore, hot formed stainless steel is not widely produced and applied.

Table 3. Chemical compositions (wt.%) of the hot-formed stainless steels [76–80].

Steel	C	Mn	Cr	Ni	Others
Max1.2	0.10	0.4	12	0	Nb
Max1.2HY	0.06	>0	11	0.5	Nb
Max2	0.2–0.25	>0.3	13	0–2	Nb
H1200PH	0.43–0.5	1.40	13.5 ± 1	0	-

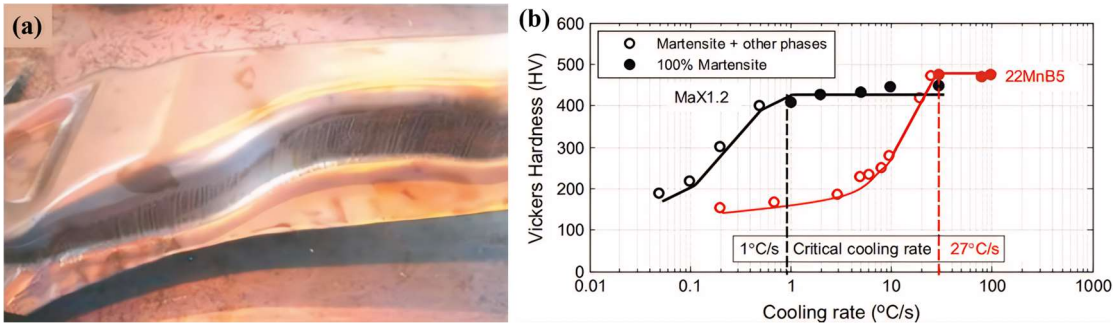

Figure 8. (**a**) Hot-formed stainless-steel B-pillar parts [77], and (**b**) Comparison of MaX1.2 and 22MnB5 critical cooling speeds [41,78].

3.2. Novel Cr-Alloyed Medium-Mn Steels

In recent years, in response to the drawbacks of poor oxidation resistance and the high cost associated with Al–Si coatings on 22MnB5 bare sheets, Luo and co-workers have developed a new Cr-alloyed medium -Mn steel (referred as "MMCr" steel, Table 4) to replace conventional PHS [81]. As demonstrated in Figure 9a, the thickness of the oxide layer of the MMCr steel is less than 3 μm following hot-stamping in air at 750–810 °C for 5 min. In comparison to the oxidation of the 22MnB5 steel (about 5 μm) at 750 °C (Figure 9e), the oxidation resistance is significantly enhanced. The enhanced oxidation resistance of MMCr steel during the hot-stamping process can be attributed to two primary factors. Firstly, the high Cr and Al contents in MMCr steel facilitate the formation of a Cr- and Al-rich oxide layer during oxidation (Figure 9b). Both Cr_2O_3 and Al_2O_3 possess the ability to mitigate the oxidation of the substrate (Figure 9c), thereby augmenting the antioxidant properties of the steel [82]. Secondly, the higher Mn content of the MMCr steel leads to a lower austenitizing temperature Ac_3 (Figure 9d), which results in a lower hot stamping temperature being used.

The novel Cr-alloyed medium-Mn steel has been demonstrated to be an effective solution to the issue of high-temperature oxidation of the bare sheet. However, it should be noted that the addition of both high Cr and high Mn content results in an elevated cost of the alloy. Furthermore, the hot stamping temperature of this alloy differs significantly from the temperature commonly utilized in current industrial production, resulting in suboptimal industrial compatibility and limited widespread utilization.

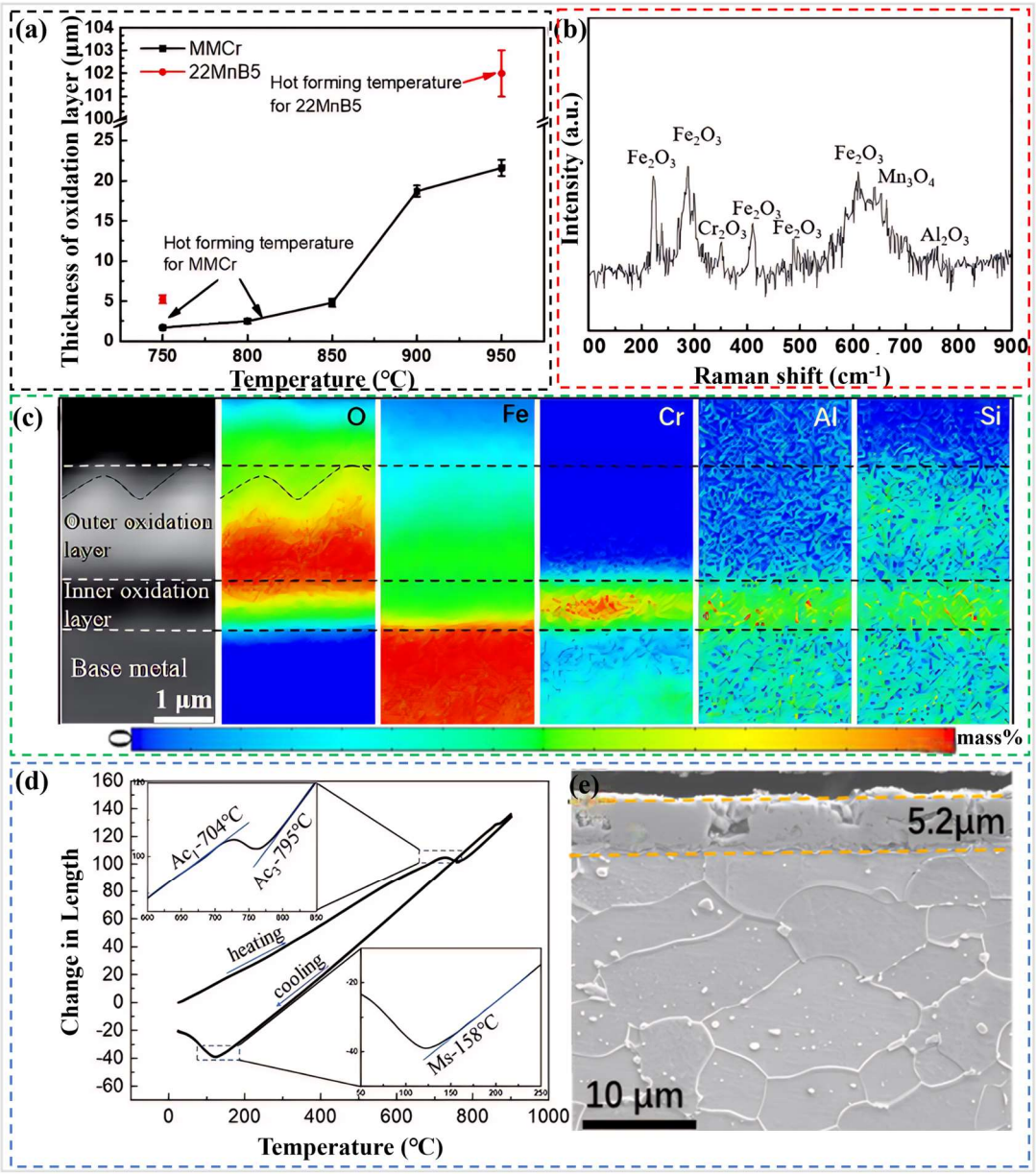

Figure 9. (**a**) Oxide layer thickness during hot stamping of MMCr steel at a different temperature, compared to 22MnB5 bare sheet, (**b**) Raman spectra of the oxide cross-section of MMCr steel at 750 °C, (**c**) The electron probe microanalyzer of elemental (EPMA) mapping of the cross-section of the oxide layer of MMCr steel after oxidation at 750 °C, (**d**) Dilatation as a function of temperature for MMCr steel, and (**e**) Cross-sectional morphology of the oxide layer of 22MnB5 bare sheet at 750 °C [81].

3.3. Novel Cr–Si Alloyed PHS

To reduce production costs and improve weldability, it is imperative to decrease the alloying content of Cr and Mn. However, it is well known that the antioxidant properties of single Cr-alloyed steels are usually directly proportional to the Cr content and that the reduction of antioxidant properties by lowering the Cr content is unavoidable. Previous literature [83–86] has demonstrated that the incorporation of a moderate amount of Si in heat-resistant steels (Cr ≥ 9 wt.%) can mitigate or even eliminate the adverse effects on their antioxidant properties resulting from decreased Cr content. This phenomenon is primarily attributed to the higher oxygen affinity and thermal stability of Si, which facilitates the formation of a protective SiO_2 healing layer and promotes the formation of a protective Cr_2O_3 layer. Consequently, a synergistic high-temperature oxidation resistance mechanism of Cr and Si is proposed in heat-resistant alloy steels [87,88]. This theoretical framework has guided numerous researchers in developing novel Cr–Si alloyed PHS [89,90]. Zhao et al. [89] discovered that the thickness of the oxide layer of the Cr–Si alloyed PHS (referred as "2000HS" steel, Table 4) developed by them was 12.4 μm after oxidation at 950 °C in the air for 5 min (Figure 10b). The thickness of the oxide layer of the conventional 22MnB5 steel was 23.6 μm under the same conditions (Figure 10a), indicating that 2000HS steel exhibits superior high-temperature oxidation resistance. The study revealed that $FeCr_2O_4$

and Fe_2SiO_4 oxides formed at the interface of the matrix during oxidation due to the presence of 3 wt.% and 1.5 wt.% of Cr and Si in the matrix, respectively (Figure 10a). These oxides not only hindered the diffusion of Fe ions but also strengthened the bonding between the oxide layer and the matrix interface. Consequently, the high-temperature oxidation resistance and the spalling resistance of the oxide layer in 2000HS steel were enhanced. Although the oxide layer of 2000HS steel is relatively thin compared to that of 22MnB5 steel, it is still in the range of teens of microns, and this oxide layer may adversely affect subsequent welding and painting processes. Therefore, the oxide layer on the surface of 2000HS steel may require further treatment, which would undoubtedly increase production costs.

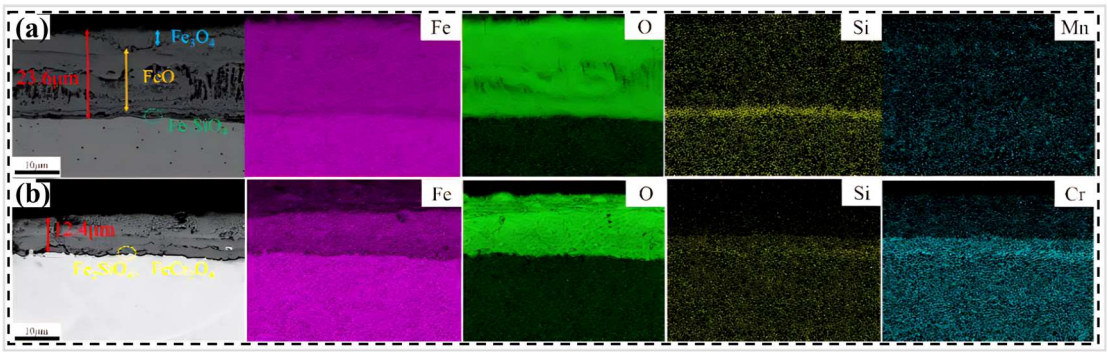

Figure 10. Cross-sectional morphology and corresponding EDS elemental analysis of conventional 22MnB5 steels (**a**) and 2000HS (**b**) at 950 °C in the air for 5 min [89].

Li et al. [91] developed a Cr–Si alloyed PHS (named as coating-free PHS: CF–PHS, Table 4) that, after oxidation for 320 s at 930 °C under N_2 conditions, formed a submicron oxide layer (0.13 μm) (Figure 11a). Under the same conditions, the oxide layer thickness of conventional 22MnB5 steel was 6.36 μm, which is almost 50 times that of the CF–PHS (Figure 11a). After oxidation, the oxide layer of the CF–PHS was mainly enriched with Cr, Mn, and Si, which were identified as Cr_2O_3, Mn_2O_3, and amorphous SiO_2 layers (Figure 11b). The continuous Cr_2O_3 and SiO_2 layers have been shown to impede the mutual diffusion of Fe and O, thereby significantly hindering the oxidation of the CF–PHS. Additionally, the Mn_2O_3 formed on the outer side of the oxide layer enhances its compactness, thereby preventing the inward invasion of O. Consequently, CF–PHS exhibited excellent high-temperature oxidation resistance. The authors believe that compared to Cr and Fe, Si and Mn have stronger oxygen affinity, which leads to the preferential formation of MnO and SiO_2 in the early oxidation stage, thereby promoting the formation of Cr_2O_3 layer, as shown in Figure 11c. Furthermore, the formation of the continuous Cr_2O_3 layer also provided time for the formation of continuous amorphous SiO_2. Due to the fact that the thickness of the oxide layer after hot stamping is only a few hundred nanometers for CF–PHS, it has been proven that shot peening is unnecessary for subsequent welding and painting processes, allowing for direct welding and painting [92], thereby reducing production costs.

Furthermore, Li et al. [93] also investigated the effect of Cr content ($Cr \leq 3$wt.%) on the high-temperature oxidation resistance of CF–PHS by oxidation under N_2 at 930 °C for 300 s. The results revealed that CF–PHS exhibited superior oxidation resistance when the Cr content reached approximately 2.5 wt.%, as illustrated in Figure 12a,b. When the Cr content is 1.5 wt.% or lower, even when Si and Mn are favorable for promoting the formation of Cr_2O_3 protective layer, a continuous Cr_2O_3 layer cannot be formed. Instead, it transforms into a less protective Fe–Cr spinel oxide, which leads to the rapid growth of Fe-oxides and, consequently, poorer oxidation resistance, as shown in Figure 12c. It is evident that there is a limited potential for optimizing the Cr content of CF–PHS from a compositional perspective to achieve additional economic benefits. Simultaneously, the exceptional oxidation resistance of CF–PHS necessitates the protection of inert gases, a factor that undoubtedly constrains their utilization. To overcome this limitation, researchers have suggested the pretreatment or incorporation of rare earth elements into CF–PHS. This approach aims to augment its high-temperature oxidation resistance, ensuring its effectiveness in unprotected atmospheres.

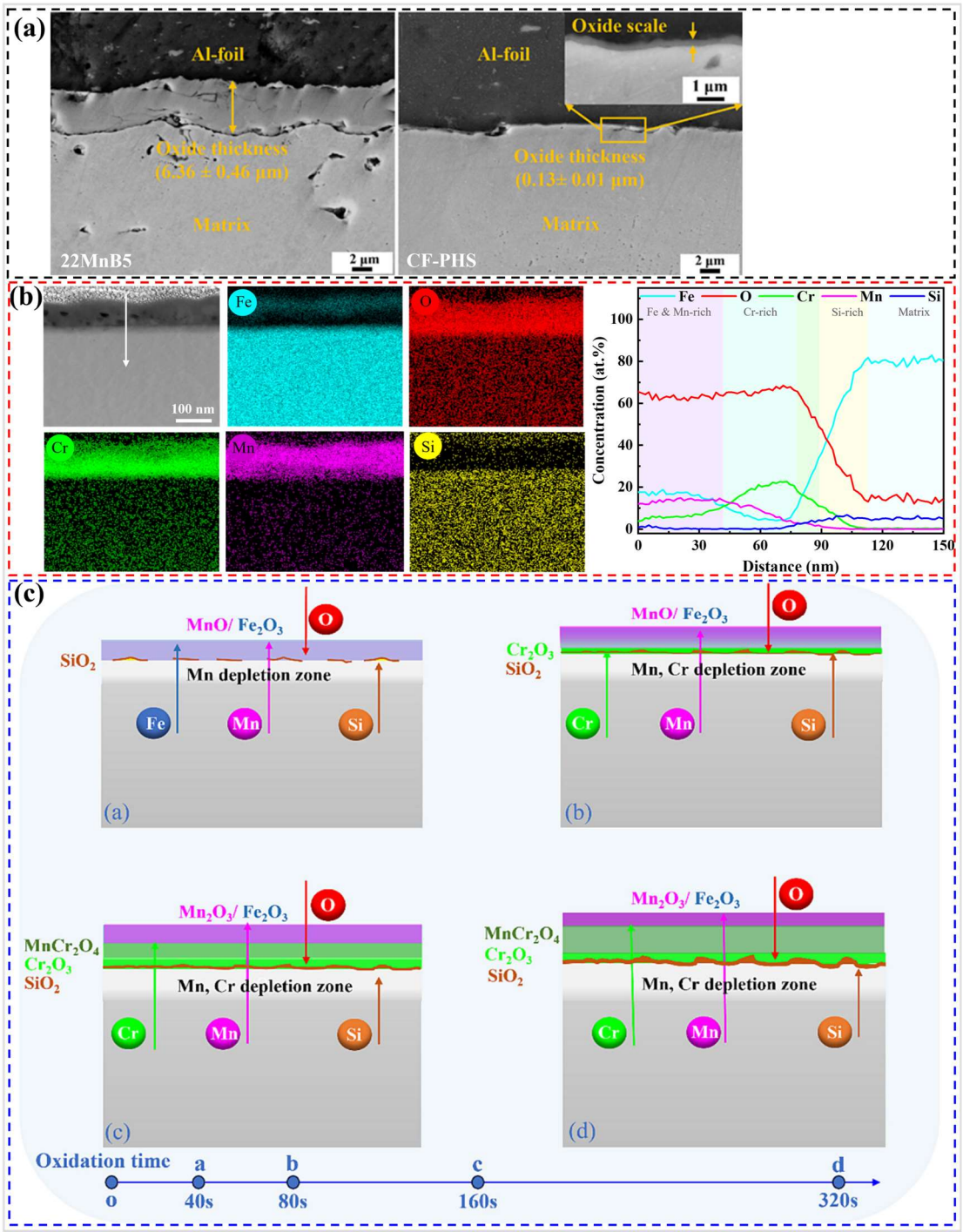

Figure 11. (**a**) Cross-sectional morphology of oxide layers of 22MnB5 and CF–PHS steels oxide at 930 °C in N_2 for 320 s, (**b**) transmission electron microscopy (TEM) morphologies and EDS elemental analyses of CF–PHS, and (**c**) Schematic diagram of the formation mechanism of the oxide layer of CF–PHS [91].

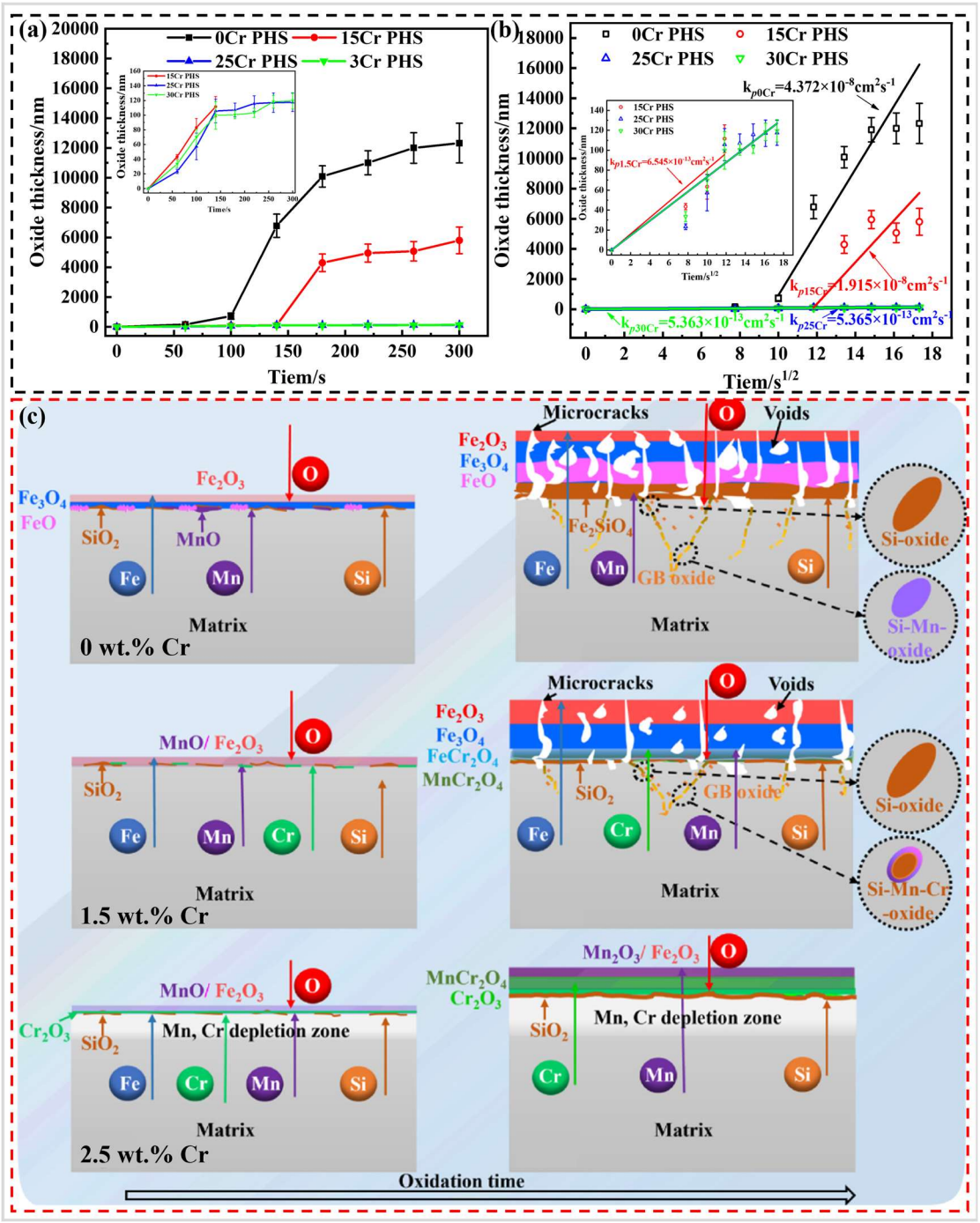

Figure 12. (**a**) Curves of oxide layer thickness with time for Cr–Si alloyed PHS with different Cr contents, (**b**) The oxidation rates obtained by fitting (0 wt.%-0Cr PHS, 1.5 wt.%-15Cr PHS, 2.5 wt.%-25Cr PHS, 3.0 wt.%-30Cr PHS), and (**c**) Schematic diagram of oxidation mechanisms for steels with different Cr contents oxidized at 930 °C for 300 s [93].

Li et al. [94] utilized temperatures of 640, 760 and 840 °C to pre-oxidize the CF–PHS in an unprotected atmosphere. The samples pre-oxidized at 760 °C were found to have an oxide layer thickness of 0.15 μm after 10 min of oxidation in air at 950 °C, showing excellent oxidation resistance similar to those in the protected atmosphere. The pre-oxidation process enhances the oxidation resistance of CF–PHS in air due to two primary mechanisms. The relative contents of Mn–Fe spinel oxides in both the 760 and 840 °C pre-oxidized films are higher than those in the 640 °C pre-oxidized films (Figure 13a). The relative contents of Mn-rich oxides in the 760 and 840 °C pre-oxidized films are also higher than those in the 640 °C pre-oxidized films (Figure 13b). Both Mn-rich oxides and spinel can promote the compactness of the oxide film, indicating that the 760 and 840 °C pre-oxidation films are more conducive to improving the subsequent oxidation resistance. Moreover, the continuous Mn–Cr spinel at the interface between the oxide layer and the matrix further improves the densification of the oxide film. Therefore, the 760 °C pre-oxidation films promoted the formation of Cr_2O_3 protective layer during the subsequent hot stamping process, which effectively improved the high-temperature oxidation resistance of CF–PHS under unprotected conditions (Figure 13d). It is evident that the selection

of the pre-oxidation temperature is pivotal in determining the optimal oxidation resistance of CF–PHS in an unprotected atmosphere, as temperatures that are excessively low or high can have a deleterious effect (Figure 13b,c,e).

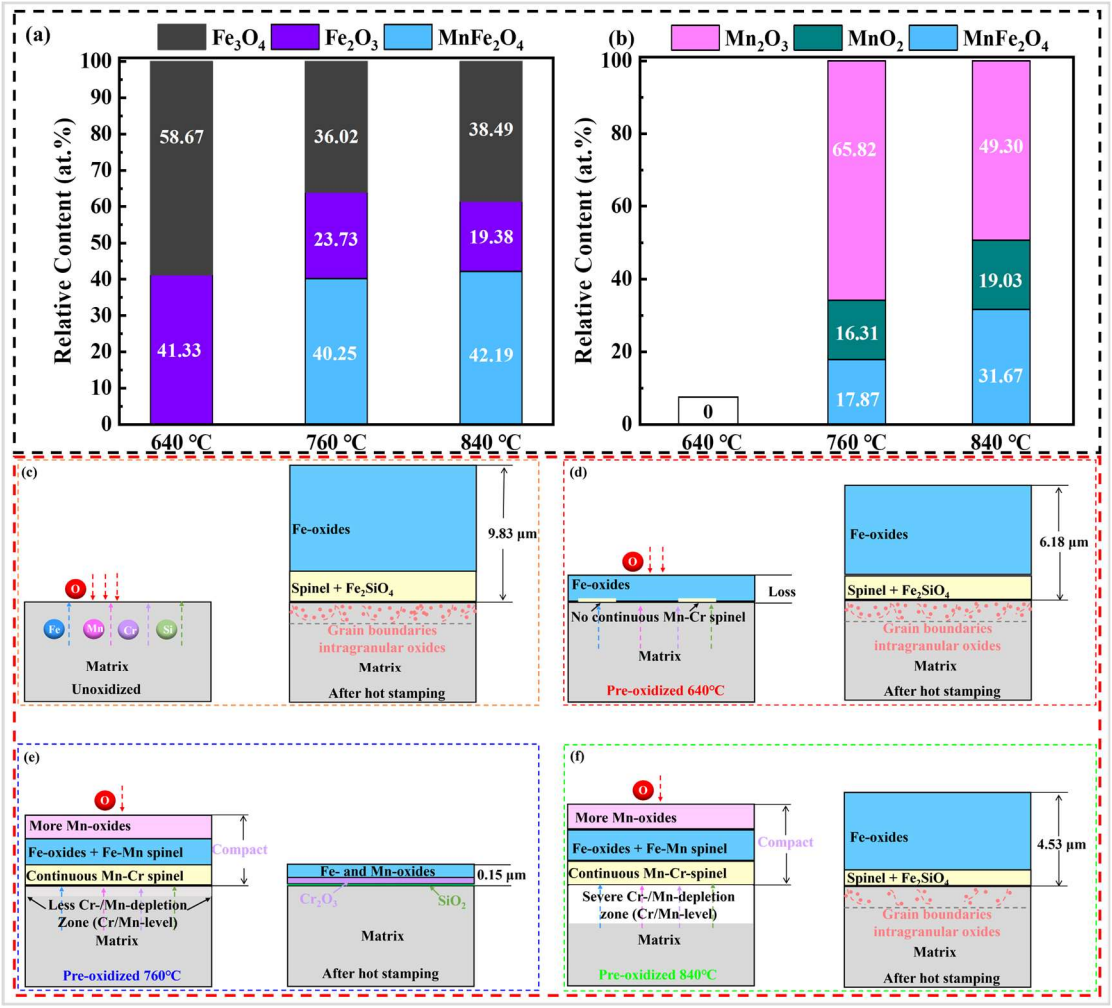

Figure 13. Relative content of each oxide in pre-oxidized films analyzed by X-ray photoelectron spectroscopy (XPS) (**a**) Fe2p, (**b**) Mn2p, (**c**) Schematic representation of oxidation before and after hot stamping of unoxidized CF–PHS, (**d**) Schematic representation of oxidation before and after hot stamping of 640 °C pre-oxidized CF–PHS, (**e**) 760 °C pre-oxidized CF–PHS, and (**f**) 840 °C pre-oxidized CF–PHS [94].

Du et al. [95] incorporated 0.024 and 0.06 wt.% of Ce into Cr–Si alloyed PHS (Table 4) and subjected them to oxidation at 950 °C in air for up to 120 min. The results indicated that the high-temperature oxidation resistance of Cr–Si alloyed PHS increased with the increase of Ce content, as shown in Figure 14a,b. The addition of Ce resulted in the formation of a thicker Cr–Si enriched layer in the initial stage of oxidation of the Cr–Si alloyed PHS (Figure 14c), which led to a denser oxide layer, and significantly reduced the degree of its oxidation. Meanwhile, Ce_2O_3 particles were segregated into the internal Cr–Si enriched layer during the oxidation process (Figure 14e), which reduced the vacancy concentration, enhanced the adhesion between the oxide layer and the matrix, and avoided the deterioration of oxidation caused by the shedding of the oxide layer. Consequently, this effectively improved the high-temperature oxidation resistance of Cr–Si alloyed PHS. In contrast, the Cr–Si alloyed PHS without added Ce exhibited more defects in the oxide layer and inferior oxidation resistance (Figure 14d). There are two other mechanisms by which rare earth elements improve the oxidation resistance of steel. (1) The addition of rare earth elements can promote the selective oxidation of Cr, resulting in the rapid formation of a protective Cr_2O_3 layer [96]. (2) Rare earths segregate to the oxide grain boundaries, which inhibit the outward diffusion of cations, and oxidation is transformed into inward diffusion of anions, resulting in a lower oxidation rate [97]. Based on the above theory, the following authors designed oxidation-resistant PHS with the addition of rare earths. Xu et al. [98] added rare earth Ce or Y to Cr–Si alloyed PHS and demonstrated that rare earth improved the oxidation resistance of Cr–Si alloyed steel during hot stamping. However, they added relatively high contents of Ce (~0.14 wt.%) and Y (~0.2 wt.%). The thickness of the oxide layer after oxidation in air at 950 °C for 10 min was less than 1 μm, and the high-temperature antioxidant properties of Cr–Si

alloyed CF–PHS were significantly improved. Zhao et al. [99,100] developed a rare-earth Y (0.003–0.007 wt.%) or Ce–containing (0.003–0.008 wt.%) uncoated PHS (Table 4) with an oxide layer thickness of less than 6 μm after oxidation in air at 930 °C for 5 min. The rare-earth uncoated PHS showed superior oxidation resistance compared to 22MnB5 (oxide layer thickness of 10.2 μm) oxidized under the same conditions.

It is evident that the high-temperature oxidation resistance of Cr–Si alloyed PHS under unprotected atmospheres can be enhanced by pre-oxidation and the addition of rare earth elements. However, further exploration is necessary to ascertain the compatibility of pre-oxidation with production requirements. It should be noted that the addition of rare earth elements will further increase production costs.

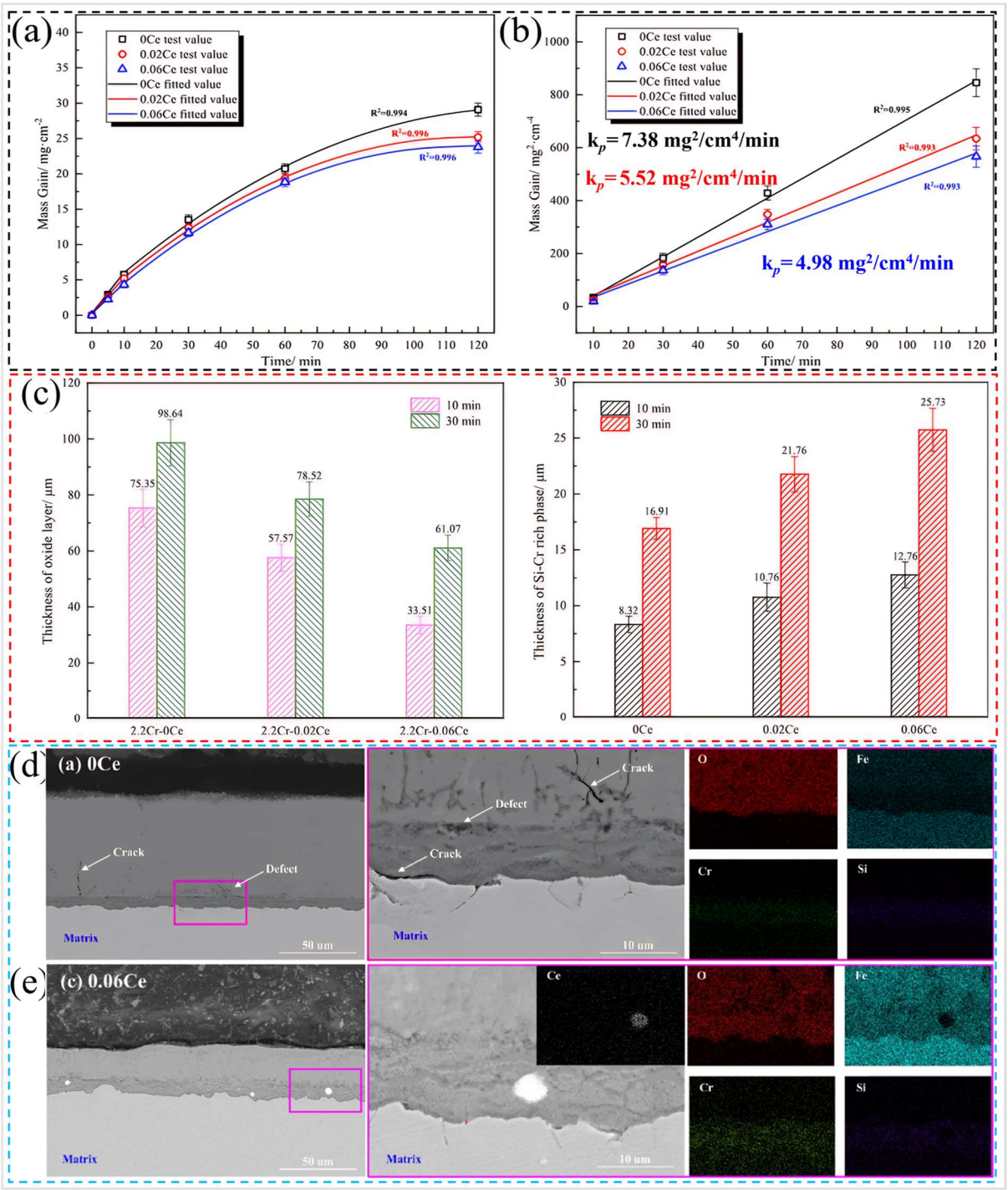

Figure 14. (**a**) Curves of mass change of different samples, (**b**) Curves of mass change squared of different samples, (**c**) Average of thickness of oxide layer and Cr–Si rich layer of different samples, Cross-sectional morphology and elemental distribution of the oxide layers of (**d**) Ce-free and (**e**) 0.06 wt.% Ce steels [95].

Ding et al. [101] developed a high-Si alloyed PHS (referred to as "HSi" steel, Table 4), which exhibited an oxide layer thickness of less than 1.6 μm on its surface after undergoing oxidation in air for 3 min at 825 °C (Figure 15a).

Under the same conditions, the oxide layer thickness of 22MnB5 steel was observed to be more than 11.2 µm, approximately 45 times higher than that of the HSi steel. This observation suggests that HSi steel possesses superior high-temperature oxidation resistance compared to 22MnB5 steel. The excellent oxidation resistance of HSi steels during hot stamping can be attributed to the lower oxidation temperature and the formation of Si- and Cr-rich oxide layers during the oxidation process (Figure 15c). These oxide layers may contain SiO_2 and Cr_2O_3 (Figure 15b), which effectively inhibit the inward diffusion of oxygen and, consequently, the oxidation of the matrix. Although the oxygen resistance of the HSi steel is enhanced compared to 22MnB5 steel, the Cr content remains relatively low. As a result, after 5 min of oxidation at 900 °C, the oxide layer thickness of HSi steel reaches about 10 µm, and its oxidation resistance becomes inferior to that of previously developed CF–PHS.

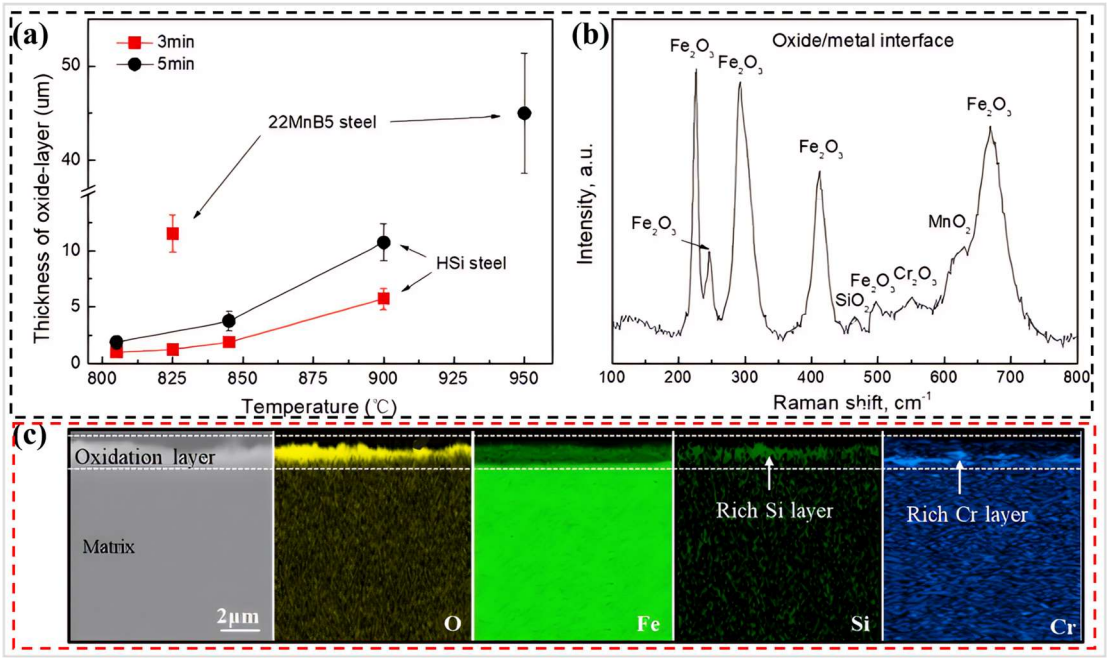

Figure 15. (**a**) Oxide layer thickness of HSi steels during the hot stamping at different temperatures and times, in comparison with 22MnB5 steel, (**b**) Raman spectra of the oxide layer of HSi steels after oxidation 825 °C for 3 min, and (**c**) Elemental distributions on the cross-section of oxide-layer formed on the HSi steels after oxidation 825 °C for 3 min, as measured by EDS [101].

3.4. Novel Si–Al Alloyed PHS

Ding et al. [102] have developed a novel Si–Al alloyed PHS (referred to as "HSiAl" steel, Table 4) that has demonstrated excellent high-temperature oxidation resistance following oxidation in air at temperatures of 820 and 950 °C for durations ranging from 5 to 120 min. As demonstrated in Figure 16a, the oxidation weight gain and oxidation rate constant values of the HSiAl steel are considerably lower than those of the conventional 22MnB5 steel under analogous conditions. The exceptional oxidation resistance of the HSiAl steel can be ascribed to the diffusion of Si and Al outward from the matrix during the initial stage of oxidation to form Al_2O_3 and SiO_2 (Figure 16b), which are dense oxides that can impede further oxidation of the matrix (Figure 16c). Despite the substitution of chromium Cr for Al in HSiAl steel, the Mn content remains comparatively elevated, and the alloying costs may not undergo substantial modification. Furthermore, the high-temperature oxidation resistance mechanism of HSiAl steel during hot stamping requires further investigation, as it is still in the experimental research and development stage.

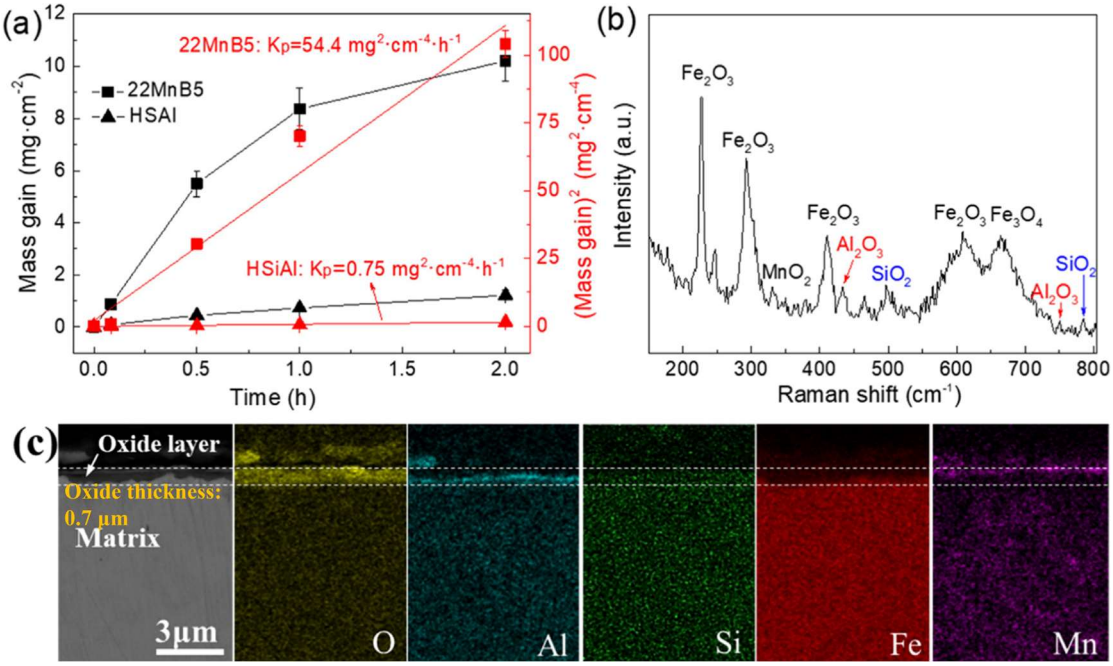

Figure 16. (**a**) Curves of mass change and fitted with the parabolic law of HSiAl steels and -22MnB5 steel in air at 820 °C, (**b**) Raman spectra of the oxide layer of HSiAl steels after oxidation 950 °C for 5 min, and (**c**) Elemental distributions on the cross-section of oxide-layer formed on the HSiAl steels after oxidation 820 °C for 5 min, as measured by EDS [102].

Table 4. Chemical compositions (wt.%) of the novel PHS.

Steel	C	Cr	Si	Mn	Al	Ce	Y	Nb	Fe	Ref.
MMCr	0.25	3.29	0.38	6.94	0.23	-	-	<0.12	Bal.	[81]
2000HS	0.35–0.40	≤3.0	≤2.0	1.10–1.50	-	-	-	≤0.026	Bal.	[89]
CF–PHS	0.196	2.46	1.51	1.38	-	-	-	0.029	Bal.	[91,92]
0Ce	0.24	2.20	1.63	1.50	0.072	-	-	-	Bal.	[95]
0.02Ce	0.24	2.18	1.62	1.51	0.076	0.024	-	-	Bal.	[95]
0.06Ce	0.24	2.19	1.60	1.51	0.070	0.060	-	-	Bal.	[95]
CF–PHS	0.196	2.46	1.51	1.38	-	≤0.14	-	0.029	Bal.	[98]
CF–PHS	0.196	2.46	1.51	1.38	-	-	≤0.2	0.029	Bal.	[99]
Uncoated PHS	0.2–0.4	0.15–1.5	1.3–2.0	1.0–1.8	≤0.05	0.003–0.008	-	-	Bal.	[99]
Uncoated PHS	0.2–0.4	0.15–1.5	1.3–2.0	1.0–1.8	≤0.05	-	0.003–0.007	-	Bal.	[100]
HSi	0.25	0.56	1.58	1.29	0.05	-	-	0.038	Bal.	[101]
HSiAl	0.26	-	1.81	3.14	1.17	-	-	0.047	Bal.	[102]

From the above discussion, oxidation-resistant PHS can be divided into two categories, one of which is hot-formed stainless steels with high Cr content, but the cost becomes an inevitable drawback. Therefore, to reduce the cost while maintaining a certain resistance to high-temperature oxidation of PHS, by reducing the alloy content and using a variety of antioxidant elements between the synergistic effect to achieve the purpose of oxidation resistance, which is the second category of novel PHS. With the addition of antioxidant alloying elements, the novel PHS has excellent high-temperature oxidation resistance during the hot stamping process and shows great potential for industrial applications.

Table 5 summarizes the high-temperature oxidation resistance of some oxidation-resistant PHS and conventional Mn–B steels during hot stamping. Although the high-temperature oxidation resistance of PHS can be improved by both pre-deposited films and alloy design compared with conventional Mn–B steels, novel PHS that can be used as replacements for conventional PHS should be considered not only in terms of their high-temperature oxidation resistance, but also in terms of their mechanical properties, corrosion properties, and cost, amongst other factors. Therefore, it is necessary to explore novel PHS that are superior in all aspects in the future.

Table 5. The high-temperature oxidation resistance of oxidation-resistant PHS and conventional Mn–B steels during hot stamping.

Steel Type	Temperature °C	Times	Atmosphere	Thickness μm	Drawback	Ref.
22MnB5 bare sheet	750–950	180–320	Air/N_2	5–23.6	Damaging die/shot peening/reduced part accuracy/ high-cost	[81,89]
Pre-deposited film-Na_2MoO_4	930	900–1800	Air	2.87–3.03	Production compatibility unknown	[70]
Pre-deposited film-silicate-molybdate	930	1200	Ar + 0.1 vol% O_2	5.9–15.4	Production compatibility unknown	[73]
MMCr	750–810	300	Air	< 3	High-cost	[81]
2000HS	950	300	Air	12.4	Poor weldability	[89]
CF–PHS	930	320	N_2	0.13	-	[91]
Ce–PHS	950	600	Air	33.51	High-cost	[95]
Uncoated PHS	930	300	Air	<6	High-cost	[99,100]
HSi	800–900	180–300	Air	≤10	Poor weldability	[101]
HSiAl	820	300	Air	0.7	High-cost	[102]

Table 5 also summarizes the comparison of the newly developed PHS, which incorporates additions of Cr and Si/Al, in terms of alloying cost, effectiveness in oxidation resistance, and weldability. The oxide layer thickness of the MMCr steels measures less than 3 μm, representing a notable enhancement in oxidation resistance when compared to the conventional 22MnB5 steel under identical conditions. Consequently, the weldability of MMCr steel is superior due to its thinner oxide layer. However, the elevated levels of Cr and Mn in MMCr steels lead to increased costs in comparison to other novel PHS. The 2000HS steels, characterized by an oxide layer thickness of 12.4 μm, exhibit improved oxidation resistance relative to 22MnB5 steels. Additionally, 2000HS steels and CF–PHS possess comparable concentrations of Cr, Si, and Mn, leading to similar alloy costs. Nevertheless, the thicker oxidation layer of 2000HS steel and its inferior weldability distinguish it from CF–PHS. The oxidation layer of CF–PHS is below 1 μm, resulting in a substantial enhancement in antioxidant properties and, consequently, better weldability. The oxidation layer thickness of HSi steel is less than 10 μm, and it demonstrates superior antioxidant properties compared to 22MnB5 steel. However, the thicker oxide layer contributes to its relatively poor weldability. HSi steels have a lower alloy content compared to other novel PHS, leading to the lowest alloy cost among them. HSiAl steels, with an oxide layer thickness of 3 μm, exhibit a significant improvement in oxidation resistance when compared to 22MnB5 steels and possess better weldability. However, the relatively high content of Al, in addition to a high Si content, in HSiAl steel results in a higher alloy cost. It is important to note that due to the varying oxidizing conditions (temperature and atmosphere) of the various novel PHS, a direct comparison of their antioxidant properties is not feasible.

Despite the significant advancements made in the field of oxidation-resistant PHS in recent years, there are still some potential research areas that merit further attention: (1) Research has predominantly concentrated on the excellent high-temperature oxidation resistance resulting from the addition of antioxidant elements. However, there is a paucity of studies examining the synergistic oxidation resistance mechanism of each alloying element at high temperatures. (2) The content of added antioxidant elements such as Cr, Si and Al is less researched. To optimize high temperature antioxidant performance and reduce cost, the ratios of antioxidation elements still need to be further studied. (3) At present, only a few the CF–PHS through industrial trials and verified that the oxide layer thickness of less than 1 μm oxide layer has good welding, phosphating and painting (good adhesion of the coating) performance [92]. Although other novel PHS have significantly reduced oxide layer thickness compared to 22MnB5 bare sheet, the effect of the oxide layer on subsequent welding, phosphating and painting is still unclear. (4) Further research is required to elucidate the effect of oxide layer thickness on other properties of the novel PHS, including corrosion properties [103], bending properties [104], wear properties [105] and hydrogen embrittlement resistance [106].

4. Cost-Effectiveness Analysis of Antioxidant Resistance in PHS

With the discussion in the above sections, this chapter compares the cost-effectiveness of coatings, pre-deposited films, and novel PHS relative to conventional Mn–B PHS. Al–Si coatings are more costly than traditional Mn–B steel bare plates due to patent limitations and problems such as coating sticking to rollers and reducing roller conveyor life. The cost of Zn-based coatings remains high relative to conventional Mn–B bare steel. Pre-deposited films to improve the oxidation resistance of PHS use sodium molybdate and sodium silicate, which are relatively inexpensive relative to coatings. The antioxidant properties of the new alloyed PHS are derived from the addition of a certain amount of antioxidant elements such as Cr, Si or Al, and therefore, the cost of the alloy is higher compared to the traditional Mn–

B steel alloys. The composition of MMCr steels consists of 3.29 wt.% Cr and 6.94 wt.% Mn (Table 4), respectively, represents a higher alloy content contributing to an elevated alloy cost. It can be inferred that a reduction in the Cr content would result in a corresponding decrement in antioxidant properties. HSiAl steel has a composition of 1.81 wt.% Si, 1.17 wt.% Al, and 3.14 wt.% Mn (Table 4) constitutes a high alloy content, resulting in a relatively high alloy cost. To achieve an optimal balance between cost and antioxidant properties in HSiAl steels, it is necessary to analyze steels with varying Si and Al contents through purposeful design. This analysis involves examining the cost and antioxidant properties of HSiAl steels with different Si and Al compositions. The 2000HS and CF–PHS steels exhibit similar contents of Cr, Si, and Mn, resulting in a lower alloy cost compared to MMCr and HSiAl steels. Reducing the Cr content to 1.5 wt.% can decrease the alloy cost but significantly impair the antioxidant properties [93]. The Cr content in HSi steels is notably lower than in CF–PHS (Table 4), leading to a lower alloy cost. The antioxidant element in HSi steels is solely Si, and a decrease in Si content would result in a lower alloy cost but also a deterioration of antioxidant properties. Furthermore, the oxidation resistance of HSi steels is inferior to those of MMCr and HSiAl steels.

5. Conclusions and Perspectives

The present review focuses on research addressing the high-temperature oxidation challenges of conventional Mn–B steels during hot stamping, using strategies such as coatings, pre-deposited films and alloy designs. In the case of coatings, the emphasis is on elucidating the anti-oxidation effects and behavioral mechanisms of diverse coatings during hot stamping while also discussing their associated merits and demerits. Regarding the strategy of pre-precipitated films, the focus lies in understanding the mechanism through which these films enhance the high-temperature oxidation resistance of PHS. The majority of alloying designs have centered on the incorporation of a single antioxidant element (Cr, Si) or a combination of two (Cr–Si/Si–Al) to bolster the high-temperature antioxidant performance of PHS. However, there has been limited research on the optimization of alloying element content and the underlying mechanisms of oxidation. Consequently, the aforementioned antioxidant strategies for PHS possess the following development potential:

(1) In the field of coatings, Zn-based coatings have exhibited exceptional antioxidant and anti-corrosion properties, thereby demonstrating superior overall performance compared to Al–Si coatings. However, the LME phenomenon poses a significant challenge, as it restricts the application of Zn-based coatings. Consequently, the present research focuses on the elimination of LME in Zn-based coatings for oxidation protective coatings in the context of PHS. The occurrence of LME necessitates the satisfaction of two conditions: the presence of liquid metal and the application of stress. The resolution of this issue can be achieved through the reduction of stress, the minimization of liquid metal, the reduction of material sensitivity, and the improvement of the process.

(2) The issue of high-temperature oxidation of PHS can be effectively addressed through the utilization of pre-deposited films. The most significant challenge pertains to the integration of this process into existing production lines. Given the use of chemicals such as sodium molybdate or sodium silicate, it is recommended to assess the feasibility of incorporating pre-deposited films into the pickling process.

(3) In terms of alloying design, given the high cost associated with the high Cr content of hot-formed stainless steel, optimizing the design of the alloying composition to improve the existing oxidation-resistant PHS is a more pragmatic approach. Further research is still required to investigate the synergistic effect of various antioxidant elements on the oxidation behavior of oxidation-resistant PHS at high temperatures, thereby providing theoretical support for the further refinement of alloy composition design. Moreover, determining how to judiciously regulate the addition of Cr, Si, Al, and other elements to reduce the cost of oxidation-resistant PHS, while maintaining excellent oxidation resistance will be a pivotal direction for the sustainable development of oxidation-resistant PHS in the future.

Acknowledgment

No specific acknowledgment except for funding sources.

Author Contributions

Z.L.: Investigation, Data curation, Formal analysis, Writing—original draft. L.W.: Methodology, Writing—review & editing, Resources. Z.W.: Validation, Writing—review & editing. J.W.: Writing—review & editing, Supervision. W.X.: Writing—review & editing, Resources, Supervision.

Ethics Statement

Not applicable.

Informed Consent Statement

Not applicable.

Data Availability Statement

Not applicable.

Funding

This work was supported by the National Natural Science Foundation of China (Grant numbers: U22A20106 and U22A20173).

Declaration of Competing Interest

The authors declare that they have no known competing financial interests or personal relationships that could have appeared to influence the work reported in this paper.

References

1. Zhao J, Jiang Z. Thermomechanical processing of advanced high strength steels. *Prog. Mater. Sci.* **2018**, *94*, 174–242.
2. Li Y, Ha N, Li T. Research on Carbon Emissions of Electric Vehicles throughout the Life Cycle Assessment Taking into Vehicle Weight and Grid Mix Composition. *Energies* **2019**, *12*, 3612.
3. Joost WJ. Reducing Vehicle Weight and Improving U.S. Energy Efficiency Using Integrated Computational Materials Engineering. *JOM* **2012**, *64*, 1032–1038.
4. Jian B. Niobium microalloying in the automotive steels for light-weighting. *SEAISI Q.* **2015**, *44*, 25–32.
5. Van Ratingen M, Williams A, Anders L, Seeck A, Castaing P, Kolke R, et al. The European New Car Assessment Programme: A historical review. *Chin. J. Trauma* **2016**, *2*, 63–69.
6. Mohd Isa MH, Ahmad Y, Abu Kassim KA, Voon WS. New Car Assessment Program for Southeast Asian Countries: Current Status and Future Developments. *Appl. Mechan. Mater.* **2014**, *564*, 54–59.
7. Zhong L, Fu P, Jing Z. The research status and development prospects of AZ31 magnesium alloy. *Met. For. Tech.* **2004**, *22*, 54–57+72.
8. Guan R, Lou H, Hui H. Development status, trends, and prospects of aluminum alloy materials. *Chin. Eng. Sci.* **2020**, *22*, 68–75.
9. Taylor T, Danks S, Fourlaris G. Dynamic tensile testing of ultrahigh strength hot stamped martensitic steels. *Steel Res. Int.* **2017**, *83*, 1600144.
10. Billur E. Hot formed steels. *Automot. Steels* **2017**, *1*, 387–411.
11. Chen YS, Lu H, Liang J, Rosenthal A, Liu H, Sneddon G, et al. Observation of hydrogen trapping at dislocations, grain boundaries, and precipitates. *Science* **2020**, *367*, 171–175.
12. Taylor T, Clough A. Critical review of automotive hot-stamped sheet steel from an industrial perspective. *Mater. Sci. Technol.* **2018**, *34*, 809–861.
13. Cheng Z, Gao M, Liu J, Wang S, Wu G, Gao J, et al. Multi-Scale Microstructural Tailoring and Associated Properties of Press-Hardened Steels: A Review. *Materials* **2023**, *16*, 3799.
14. Soleimani M, Kalhor A, Mirzadeh H. Transformation-induced plasticity (TRIP) in advanced steels: A review. *Mater. Sci. Eng. A.* **2020**, *795*, 140023.
15. Santacreu PO, Badinier G, Moreau JB, Herbelin JM. Fatigue properties of a new martensitic stainless steel for hot stamped chassis parts. *SAE Technical Paper* 2015. Available online: https://www.sae.org/publications/technical-papers/content/2015-01-0527/ (accessed on 25 February 2025).
16. Jin X, Gong Y, Han X, Du H, Ding W, Zhu B, et al. A Review of Current State and Prospect of the Manufacturing and Application of Advanced Hot Stamping Automobile Steels. *Acta Metall. Sin.* **2020**, *56*, 411–428.
17. Tong C, Rong Q, Yardley VA, Li X, Luo J, Zhu G, et al. New developments and future trends in low-temperature hot stamping technologies: A review. *Metals* **2020**, *10*, 1652.
18. Chai Z, Lu Q, Hu J. Effect of retained austenite on the fracture behavior of a novel press-hardened steel. *J. Mater. Sci. Tech.* **2023**, *1*, 34–45.
19. Cheng Z, Wang S, Liu J, Wu R, Gao J, Wu H, et al. Precipitation behaviour and strengthening mechanisms of V-bearing 1800

MPa grade hot-stamping steel. *Mater. Sci. Technol.* **2023**, *1*, 1–16.
20. Hu P, Ying L, Li Y, Liao Z. Effect of oxide scale on temperature-dependent interfacial heat transfer in hot stamping process. *J. Mater. Process. Technol.* **2013**, *213*, 1475–1483.
21. Kim C, Cho S, Yang W, Karayan AI, Castaneda H. Corrosion behavior of Al-Si-Mg coated hot-press-forming steel. *Corros. Sci.* **2021**, *183*, 109339.
22. Gui X, Liang K, Zhang S. Formability of aluminum-silicon coated boron steel in hot stamping process. *Trans. Nonferrous Metals Soc. China* **2014**, *24*, 1750–1757.
23. Yao Z, Ma F, Liu Q, Zhao F, Li F, Lin J, et al. High temperature oxidation resistance and mechanical properties of uncoated ultrahigh-strength steel 22MnB5. In *Proceedings of the FISITA 2012 World Automotive Congress*; Springer: Heidelberg/Berlin, Germany, 2013; pp. 67–78.
24. Wang X, Ai R, Yang Q, Wang S, Zhang Y, Meng Y, et al. Effect of oxide scale structure on shot-blasting of hot-rolled strip steel. *J Mater. Sci.* **2020**, *2*, 9–27.
25. Kennedy D, Vahey J, Hanney D. Micro shot blasting of machine tools for improving surface finish and reducing cutting forces in manufacturing. *Mater. Des.* **2005**, *26*, 203–208.
26. Bagherifard S, Ghelichi R, Guagliano M. Numerical and experimental analysis of surface roughness generated by shot peening. *Appl. Surf. Sci.* **2012**, *258*, 6831–6840.
27. Singh G, Singh S, Prakash C, Ramakrishna S. On investigating the soda-lime shot blasting of AZ31 alloy: effects on surface roughness, material removal rate, corrosion resistance, and bioactivity. *J. Magnes. Alloy.* **2021**, *9*, 1272–1284.
28. Wang Z, Lu Q, Cao ZH, Chen H, Huang MX, Wang JF. Review on hydrogen embrittlement of press-hardened steels for automotive applications. *Acta Metall. Sin.* **2023**, *36*, 1123–1143.
29. Li YJ, Ponge D, Choi P, Raabe D. Segregation of boron at prior austenite grain boundaries in a quenched martensitic steel studied by atom probe tomography. *Scr. Mater.* **2015**, *96*, 13–16.
30. Sharma M, Ortlepp I, Bleck W. Boron in heat-treatable steels: A review. *Steel Res. Int.* **2019**, *90*, 1900133.
31. Taylor T, Fourlaris G, Clough A. Effect of carbon and microalloy additions on hot stamped boron steel. *Mater. Sci. Technol.* **2017**, *33*, 1964–1977.
32. Fan W, De C. State of the knowledge on coating systems for hot stamped parts. *Steel Res. Int.* **2012**, *83*, 412–433.
33. Jenner F, Walter ME, Mohan Iyengar R, Hughes R. Evolution of Phases, Microstructure, and Surface Roughness during Heat Treatment of Aluminized Low Carbon Steel. *Metall. Mater. Trans. A* **2010**, *41*, 1554–1563.
34. Múnera DD, Pic A, Abou-Khalil D, Shmit F, Pinard F. Innovative Press Hardened Steel Based Laser Welded Blanks Solutions for Weight Savings and Crash Safety Improvements. *SAE Inter. J. Mater. Manu.* **2008**, *1*, 472–479.
35. Hein PJ. A Global Approach of the Finite Element Simulation of Hot Stamping. *Advan. Mater. Res.* **2005**, *6*, 763–770.
36. Billur E, Wang C, Bloor C, Holecek M, Porzner H, Altan T. Advancements in tailored hot stamping simulations: Cooling channel and distortion analyses. In *Proceedings of the Numisheet*, *AIP Conference Proceedings*; American Institute of Physics: College Park, MD, USA, 2014; pp. 1079–1084.
37. Vietoris T. New developments in PHS: materials, coatings, production methods. In Proceedings of the AP&T Press Hardening, Next Step Seminar, Novi, MI, USA, October 2011.
38. Grauer SJ, Caron EJ, Chester NL, Wells MA, Daun KJ. Investigation of melting in the Al–Si coating of a boron steel sheet by differential scanning calorimetry. *J. Mater. Processing Tech.* **2015**, *216*, 89–94.
39. Jhajj K. Heat Transfer Modeling of Roller Hearth and Muffle Furnace. Master's Thesis, University of Waterloo, Waterloo, ON, Canada, 2015.
40. Zhang J, Jiang SM, Zhang QF, Liu CS. Effect of temperature on microstructure and formability of Al-10 mass% Si coatings. *J. Iron Steel Res. Int.* **2016**, *23*, 270–275.
41. Billur E. *Hot Stamping of Ultra High-Strength Steels: From a Technological and Business Perspective*, 1st ed.; Springer International Publishing: Cham, Switzerland, 2019; pp. 225–245.
42. Xun Y, Qi Z. Microstructure Evolution of Hot-Dip Al–10%Si Coating During the Austenitization of 22MnB5 Hot Stamping Steel. *Acta Metall. Sin.* **2017**, *53*, 1495–1503.
43. Chang Y, Tsaur C, Rock C. Microstructure studies of an aluminide coating on 9Cr–1Mo steel during high temperature oxidation. *Surf. Coat. Technol.* **2006**, *200*, 6588.
44. Borsetto F, Ghiotti A, Bruschi S. Investigation of the high strength steel Al– Si coating during hot stamping operations. *Key Eng. Mater.* **2009**, *410*, 289–296.
45. Young J. *High Temperature Oxidation and Corrosion of Metals*, 1st ed.; Elsevier: Oxford, UK, 2008; p. 16.
46. Liu H, Lu X, Jin X, Dong H, Shi J. Enhanced mechanical properties of a hot stamped advanced high-strength steel treated by quenching and partitioning process. *Scr. Mater.* **2011**, *64*, 749–752.
47. Ma N, Hu P, Guo W. Experiments and analysis of relations among heat, stress and transformation of boron steel for hot forming. *Tran. Mater. Heat Trea.* **2010**, *12*, 33–40.
48. Schwartz R, Lehmann H. Developments in the field of heat treatment systems for hot-form hardening lines. In Proceedings of the 2nd International Conference on Hot Sheet Metal Forming of High-Performance Steel (CHS2), Lulea, Sweden, 15–17

June 2009; pp. 15–17.
49. Wang Z, Cao H, Wang F, Huang X. Improving the bending toughness of Al-Si coated press-hardened steel by tailoring coating thickness. *Scr. Mater.* **2021**, *192*, 19–25.
50. Hong Y, Chang Z, Zhao L, Da Y. Hot Stamped Component, Precoated Steel Sheet Used for Hot Stamping and Hot Stamping Process. United States Patent US 11667988, 14 February 2023.
51. Yi H, Chang Z, Liu Z. Hot Stamped Component, Pre-Coated Steel Plate for Hot Stamping, and Hot Stamping Process. World Intellectual Property Organization Patent WO2019/205698 A1, 13 October 2019.
52. Yi H, Chang Z, Cai H, Du P, Yang D. Strength, Ductility and Fracture Strain of Press-Hardening Steels. *Acta Metall. Sin.* **2020**, *56*, 429–443.
53. Belanger P. The future for press hardening in the automotive industry. In Proceedings of the AP&T Press Hardening, Next Step Seminar, Novi, MI, USA, October 2011.
54. Lee CW, Fan DW, Sohn IR, Lee SJ, De Cooman BC. Liquid-metal-induced embrittlement of Zn–coated hot stamping steel. *Metall. Mater. Trans. A* **2012**, *43*, 5122–5127.
55. Fleischanderl M, Kolnberge Sr, Faderl J. Method for producing a hardened steel part. United States Patent US 8021497, 20 September 2011.
56. American Society of Metals. *ASM Handbook of Corrosion*; ASM International: Materials Park, OH, USA, 1992.
57. Kim G. Quality evaluation of Zn coated hot press forming steel. In Proceedings of the Materials in Car Body Engineering, Bad Nauheim, Germany, 7–8 May 2013.
58. Ghatei-Kalashami A, Khan MS, Goodwin F, Zhou YN. Investigating zinc-assisted liquid metal embrittlement in ferritic and austenitic steels: correlation between crack susceptibility and failure mechanism. *Mater. Character.* **2023**, *195*, 112502.
59. Drillet P, Grigorieva R, Leuillier G, Vietoris T. Memorie Study of cracks propagation inside the steel on press hardened steel zinc based coatings. *La Metall. Ital.* **2012**, *104*, 3–8.
60. Bhattacharya D, Cho L, Van der Aa E, Ghassemi-Armaki H, Pichler A, Findley KO, Speer JG. Transgranular cracking in a liquid Zn embrittled high strength steel. *Scr. Mater.* **2020**, *175*, 49–54.
61. Dohie S, Cahoon R, Caley F. The Grain-Boundary Diffusion of Zn in α–Fe. *J. Phs. Eqil. and Diff.* **2007**, *28*, 322–327.
62. Bhattacharya D, Cho L, Van Der Aa E, Pichler A, Pottore N, Ghassemi-Armaki H, et al. Influence of the starting microstructure of an advanced high strength steel on the characteristics of Zn–Assisted liquid metal embrittlement. *Mater. Sci. Eng. A* **2021**,*15*, 140391.
63. Cho L, Kang H, Lee C, De Cooman BC. Microstructure of liquid metal embrittlement cracks on Zn–coated 22MnB5 press-hardened steel. *Scr. Mater.* **2014**, *1*, 25–28.
64. Kurz T. New developments in zinc coated steel for press hardening. In Proceedings of the Insight Edition Conference, Gothenburg, Sweden, 20–21 September 2011.
65. Allely C, Petitjean J, Vietoris T. Corrosion resistance of zinc based and aluminized coatings on press-hardened steels for automotive. In Proceedings of the 3rd International Conference on Hot Sheet Metal Forming of High Performance Steel (CHS2), Kassel, Germany, 13–17 June 2011; pp. 153–160.
66. Song M, Kim H, Lee S. Effect of a Zn interlayer on the adhesion strength and corrosion resistance of Zn–Mg coated trip steel. *ISIJ Int.* **2019**, *15*, 1113–1118.
67. Frenzer G. Nano–x gmbh x-tec® and alsi® coat products against scale formation on steel. Presentation at Nano-X, Saarbrücken, Germany, 7 April 2015.
68. Fristad W. New coil-applied coating for press-hardening steel. In Proceedings of the Galvatech, Toronto, Canada, 31 May–4 June 2015; pp. 892–898.
69. Mori K, Ito D. Prevention of Oxidation in Hot Stamping of Quenchable Steel Sheet by Oxidation Preventive Oil. *CIRP Annals-Manu. Tech.* **2009**, *58*, 267.
70. Du W, Liu C, Yue Y. Effect of passivation on the high-temperature oxidation behavior of hot-formed steel. *Corros. Sci.* **2022**, *202*, 110318.
71. Liu XJ, Cao GM, He YQ, Jia T, Liu ZY. Effect of temperature on scale morphology of Fe–1.5Si alloy. *J. Iron Steel Res.* **2013**, *20*, 73–78.
72. Lashin A. Oxidation of silicon from an Fe–6 at% Si alloy. *J. Alloys Compd.* **2013**, *567*, 54–68.
73. Nie J, Yang X, Zhao Z, Fu Y, Liu Z, Li X, et al. An innovative strategy against oxide spallation of hot formed steels. *Corros. Sci.* **2025**, *242*, 112554.
74. Martínez-González LG, Rodríguez-Reyna E, Moreno KJ, Escalante-García JI, Fuentes AF. Ionic conductivity of apatite-type rare-earth silicates prepared by mechanical milling. *J. Alloys Compd.* **2009**, *476*, 710–714.
75. Liu Z, Yu Q, Zhao Y, He R, Xu M, Feng S, et al. Silicon oxides: a promising family of anode materials for lithium-ion batteries. *Chem. Soc. Rev.* **2019**, *48*, 285–309.
76. Fröhlich T. Maximum safety and lightweight potential due to use of new high strength steels. Presented at Outokumpu Experience, London, UK, 22–23 May 2013.
77. Mori KI, Bariani PF, Behrens BA, Brosius A, Bruschi S, Maeno T, et al. Hot stamping of ultra-high strength steel parts. *Cirp*

Ann. **2017**, *66*, 755–777.
78. Herbelin J. 1000–2000 MPa Martensitic stainless steels for flexible hot forming processes. Presented at Materials in Car Body Engineering, Bad Nauheim, Germany, 13–14 May 2014.
79. Badinier G, Mithieux J, Santacreu P, Herbelin JM. Development of a 1.8 GPa martensitic stainless steel for hot stamping application. In Proceedings of the 5th International Conference on Hot Sheet Metal Forming of High Performance Steel, CHS2, Toronto, ON, Canada, 31 May–3 June 2015, pp. 715–723.
80. Badinier G, Moreau J, Petit B. Development of press hardening stainless steels for body-in-white application. In Proceedings of the 6th International Conference on Hot Sheet Metal Forming of High Performance Steel, CHS2, Atlanta, GA, USA, 4–7 June 2017, pp. 77–84.
81. Li S, Wen P, Li S, Song W, Wang Y, Luo H. A novel medium–Mn steel with superior mechanical properties and marginal oxidization after press hardening. *Acta Mater.* **2021**, *205*, 116567.
82. Chen G, Giron-Palomares B, Sun H, Wang H, Zhang Y, Duan L, et al. Effect of alloying with Al and Cr on the microstructure, damping capacity and high-temperature oxidation behaviors of Fee17Mn damping alloys. *J. Alloys Compd.* **2020**, *819*, 153035.
83. Liang Z, Göken M, Lorenz U, Neumeier S, Oehring M, Pyczak F, et al. Influence of small amounts of Si and Cr on the high temperature oxidation behavior of novel cobalt base superalloys. *Corros. Sci.* **2021**, *184*, 109388.
84. Moon J, Kim S, Park WD, Kim TY, McAlpine SW, Short MP, et al. Initial oxidation behavior of Fe–Cr–Si alloys in 1200 °C steam. *J. Nucl. Mater.* **2019**, *513*, 297–308.
85. He J, Luan Y, Guo H, Peng H, Zhang Y, Zhang T. The role of Cr and Si in affecting high-temperature oxidation behaviour of minor Dy doped NiAl alloys. *Corros. Sci.* **2013**, *77*, 322–333.
86. Wang J, Lu S, Rong L, Li D, Li Y. Effect of silicon on the oxidation resistance of 9wt.% Cr heat resistance steels in 550 °C lead-bismuth eutectic. *Corros. Sci.* **2016**, *111*, 13–25.
87. Zhang L, Yan W, Shi Q, Li Y, Shan Y, Yang K. Silicon enhances high temperature oxidation resistance of SIMP steel at 700 °C. *Corros. Sci.* **2020**, *167*, 108519.
88. Wang S, Wu Y, Ni CS, Niu Y. The effect of Si additions on the high temperature oxidation of a ternary Ni–10Cr–4Al alloy in1atm O_2 at 1100 °C. *Corros. Sci.* **2009**, *51*, 511–517.
89. Zhao Y, Yang D, Qin Z, Chu X, Liu J, Zhao Z. A novel hot stamping steel with superior mechanical properties and antioxidant properties. *J. Mater. Res. Technol.* **2022**, *21*, 1944–1959.
90. Lu Q, Pang J, Wang J. Steel for hot stamping with enhanced oxidation resistance. World Intellectual Property Organization Patent WO2019127240A1, 25 March 2019.
91. Li Z, Wang L, Wang Z, Zhang T, Wang J, Xu W. Oxidation mechanisms of a Cr-Si alloyed coating-free press-hardened steel under simulated press hardening conditions. *Mater. Character.* **2023**, *206*, 113446.
92. Chai Z, Lu Q, Tedesco S, Shi M, Coryell J, Reini L, et al. Investigation on mechanical properties and oxidation behavior of 1.2 and 1.7 GPa grades coating-free press-hardened steels. *Metals* **2023**, *13*, 489.
93. Li Z, Chai Z, Wang L, Wang Z, Lu Q, Wang J. Effect of Cr on high-temperature oxidation resistance of Cr–Si–Mn alloyed press-hardened steel during press hardening. *J. Mater. Res. Tech.* **2024**, *32*, 1552–1564.
94. Li Z, Wang L, Wang Z, Wang J, Xu W. Superior oxidation resistance in air during hot stamping of a coating-free press-hardened steel achieved by pre-oxidation. *J. Mater. Res. Tech.* **2024**, *33*, 6023–6034.
95. Du W, Liu C, Liu H, Yue Y, Zhang B. A new insight into the mechanism of Ce enhancing high temperature oxidation resistance of hot-formed steel. *J. Mater. Res. Tech.* **2024**, *28*, 2800–2814.
96. Zhang XH, Zhang C, Zhang YD, Salam S, Wang HF, Yang ZG. Effect of yttrium and aluminum additions on isothermal oxidation behavior of Tribaloy T–700 alloys. *Corro. sci.* **2014**, *1*, 405–415.
97. Tawancy HM, Abbas NM. An analytical electron microscopy study of the role of La and Y during high-temperature oxidation of selected Ni–base alloys. *Scr. Metall. Materi.* **1993**, *1*, 29.
98. Xu W, Li Z, Wang L, Jun H. A high-temperature oxidation-resistant hot stamping steel containing rare earth elements and hot stamping forming process. Chinese Patent CN202310886845.4, 29 August 2023.
99. Zhao Y, Liu L, Sun D, Wang J, Wang W, Gui T. An uncoated anti-temperature oxidation hot stamping forming steel with added Ce element. Chinese Patent CN202210192313.6, 27 May 2022.
100. Zhao Y, Liu L, Sun D, Wang J, Wang W, Gui T. An uncoated high-temperature oxidation-resistant hot stamping and forming steel with Y element. CN202210192312.1, 31 May 2022.
101. Ding C, Hu K, Chen H, Hu B, Luo H. A dual-phase press-hardening steel with improved mechanical properties and superior oxidation resistance. *Metall. and Mater. Trans. A* **2022**, *53*, 1934–1944.
102. Ding C, Zhao H, Hu B, Xu D, Ge R, Deng C, et al. A novel tri-phase lightweight press-hardening steel exhibiting both excellent mechanical properties and outstanding oxidization resistance. *J. Mater. Sci. Tech.* **2024**, *196*, 171–182.
103. Autengruber R, Luckeneder G, Hassel W. Corrosion of press-hardened galvanized steel. *Corros. Sci.* **2012**, *63*, 12–19.
104. Ding W, Yu G, Qi L, Jeff W, Zijian W, Wei Li. Improve bendability of a Cr–alloyed press-hardening steel through an in-line quenching and non-isothermal partitioning process. *J. Manuf. Process.* **2022**, *84*, 481–493.
105. Merklein M, Michael W, Michael L, Stefania B, Andrea G. Hot stamping of boron steel sheets with tailored properties: A

review. *J. Mater. Process. Technol.* **2016**, *228*, 11–24.
106. Ding W, Kai Y, Yu G, Li W, Ji-yao H, Wei L, et al. Improving hydrogen embrittlement resistance of a modified press hardening steel by introducing retained austenite as hydrogen trap. *J. Iron Steel Res. Int.* **2022**, *29*, 1864–1872.